






## Reynolds-number effects on the outer region of adverse-pressure-gradient turbulent boundary layers

Rahul Deshpande <sup>1,\*</sup>,† Aron van den Bogaard <sup>1,2,\*</sup> Ricardo Vinuesa <sup>3</sup>  
Luka Lindić <sup>1</sup> and Ivan Marusic <sup>1</sup>

<sup>1</sup>*Department of Mechanical Engineering, University of Melbourne, Parkville, Victoria 3010, Australia*

<sup>2</sup>*Physics of Fluids Group, University of Twente, P.O. Box 217, 7500AE Enschede, Netherlands*

<sup>3</sup>*FLOW, Engineering Mechanics, KTH Royal Institute of Technology, Stockholm, 10044, Sweden*



(Received 17 April 2023; accepted 13 November 2023; published 11 December 2023)

We study the Reynolds-number effects on the outer region of moderate adverse-pressure-gradient (APG) turbulent boundary layers (TBLs) and find that their small-scale (viscous) energy reduces with increasing friction Reynolds number ( $Re_\tau$ ). The trend is based on analyzing APG TBL data across  $600 \lesssim Re_\tau \lesssim 7000$  and contrasts with the negligible variation in small viscous-scaled energy noted for canonical wall flows. The data sets considered include those from a well-resolved numerical simulation [Pozuelo *et al.*, *J. Fluid Mech.* **939**, A34 (2022)], which provides access to an APG TBL maintained at near-equilibrium conditions across  $1000 \lesssim Re_\tau \lesssim 2000$ , with a well-defined flow history, and a new high- $Re_\tau$  ( $\sim 7000$ ) experimental study from the large Melbourne wind tunnel, with its long test section modified to permit development of an APG TBL from a “canonical” upstream condition. The decrease in small-scale energy with  $Re_\tau$  is revealed via decomposing the streamwise normal stresses into small- and large-scale contributions, based on a sharp spectral cutoff. The origin for this trend is traced back to the production of turbulent kinetic energy in an APG TBL, the small-scale contribution to which is also found to decrease with  $Re_\tau$  in the outer region. The conclusion is reaffirmed by investigating attenuation of streamwise normal stresses due to changing spatial resolutions of the numerical grid or hotwire sensors, which reduces with increasing  $Re_\tau$  and is found to be negligible at  $Re_\tau \sim 7000$  in this study. The results emphasize that new scaling arguments and spatial-resolution corrections should be tested rigorously across a broad  $Re_\tau$  range, particularly for pressure gradient TBLs.

DOI: [10.1103/PhysRevFluids.8.124604](https://doi.org/10.1103/PhysRevFluids.8.124604)

### I. INTRODUCTION

Turbulent boundary layers (TBLs) have been a topic of active research for over a century, considering their relevance to many engineering and scientific applications. Despite such dedicated efforts, progress has been slow owing to the unique complexities (in the form of parametric dependencies) associated with each application. While the Reynolds number is the sole parameter influencing the flow physics for incompressible, zero-pressure-gradient (ZPG) and smooth-wall (i.e., canonical) TBLs, wall-bounded flows found in nature are almost always exposed to noncanonical complexities, bringing dependence on additional parameters [1,2]. In the present study, we limit our focus to smooth-wall boundary layers exposed to an adverse-pressure gradient (APG), which are commonly found over airplane wings and turbine blades, in diffusers, as well as in many other applications.

\*These authors contributed equally to this work.

†[raadeshpande@gmail.com](mailto:raadeshpande@gmail.com)

Apart from the friction Reynolds number ( $\text{Re}_\tau$ ), previous studies have found the APG strength as well as its upstream history to influence the smooth-wall APG TBL characteristics. Following Vinuesa *et al.* [3], here  $\text{Re}_\tau = \delta_{99} U_\tau / \nu$ , where  $\delta_{99}$  is the TBL thickness,  $U_\tau$  is the friction velocity, and  $\nu$  is kinematic viscosity. For a statistically two-dimensional mean flow, the strength of the pressure gradient at a given streamwise location  $x$  is typically quantified by the Clauser pressure-gradient parameter,  $\beta(x) = (\delta^* / \rho U_\tau^2) (dP/dx)$  [1,4], where  $\delta^* = \int_0^{\delta_{99}} [1 - U(z)/U_e] dz$  is the displacement thickness,  $U(z)$  is the mean streamwise velocity at wall-normal location  $z$ ,  $U_e = U(z = \delta_{99})$ , i.e., the edge velocity,  $\rho$  is the fluid density, and  $dP/dx$  is the mean streamwise pressure gradient at  $x$ . The influence of these additional parameters makes the APG TBL characteristics inconsistent with some popular scaling arguments based on canonical wall flows. For example, the mean streamwise velocity profiles for an APG TBL have been reported to deviate from the classical log law [5–7]. The APG also reduces the wall-normal extent of the log region, which is accompanied by the increased size of its wake region [2,8,9]. Most of these changes can be associated with modifications in the inherent structure of the turbulent flow on exposure to an APG [10–12]. These modifications are made evident by the wall-normal variation of the streamwise normal stress, which is given by the variance of the streamwise velocity fluctuations ( $\overline{u^2}$ ). In the case of ZPG TBLs,  $\overline{u^2}$  profiles have the most prominent peak in the inner region of the TBL (referred henceforth as the inner peak), with the maximum  $\overline{u^2}$  values in the outer region much lower than the inner peak at low-to-moderate  $\text{Re}_\tau$  [13]. In contrast, APG TBLs in a similar  $\text{Re}_\tau$  range but with a reasonably strong  $\beta$  will exhibit a distinct local maximum of  $\overline{u^2}$  in the outer region (i.e., an outer peak), which can be larger than the inner peak [9,14,15]. This prominent outer peak is associated with enhanced contributions from the large as well as small scales, as compared to a ZPG TBL [8,9,16]. Such unique observations have motivated the proposal of new scaling arguments for the outer region of APG TBLs [1,17–23], which, however, are based on a limited parameter space. What is ideally desired is a universal scaling that can account for the multiparameter dependence [2], as comprehensively as that noted previously for canonical flows [5,6,24,25].

Establishment of scaling laws, inevitably, is preceded by a thorough understanding of the influence of various parameters on the flow characteristics. This is the primary aim of the present study, which limits its focus to the outer region ( $z^+ = zU_\tau/\nu \gtrsim 100$ ) of a smooth wall TBL exposed to a moderate APG ( $\beta \lesssim 2$ ), a regime which has not been extensively studied, despite its importance [26]. The present discussion is also limited to three parameters— $\text{Re}_\tau$ ,  $\beta(x)$ , and upstream history of  $\beta$  [i.e.  $\overline{\beta}(x)$ ]—which have been investigated systematically by multiple studies [11,15,27–30]. Their findings have significantly advanced our understanding of the outer region and have been summarized in Table I for convenience. Here  $\overline{\beta}(x)$  is used to quantify upstream flow-history effects [31,32] and is estimated by

$$\overline{\beta}(x) = \frac{\int_{\text{Re}_{\theta,x=0}}^{\text{Re}_{\theta,x}} \beta(\text{Re}_{\theta,x}) d\text{Re}_{\theta,x}}{\text{Re}_{\theta,x} - \text{Re}_{\theta,x=0}}, \quad (1)$$

where  $\text{Re}_\theta$  corresponds to the Reynolds number based on momentum thickness ( $=\theta U_e/\nu$ ). It is important to note here that an APG TBL can also be characterized by several other parameters [2,5,8,14,15,17,27,33,34], most of which have been historically used to quantify equilibrium or self-preserving aspects of these TBLs, which is beyond the scope (and focus) of this study. Here we discuss the effects of the three selected parameters on the small-scale ( $\lambda_y \leq \lambda_{y,c}$ ) and large-scale ( $\lambda_y > \lambda_{y,c}$ ) energy (Table I), where  $\lambda_{y,c}$  corresponds to a representative spanwise wavelength cutoff for segregating these scales (with  $\lambda_y = 2\pi/k_y$ ;  $k_y$  being the spanwise wave number). Throughout this paper, by small scales, we are essentially referring to the fine dissipative scales and the viscous-scale contribution to  $\overline{u^2}$ , whereas large scales correspond to the contribution from inertial scales (i.e., attached eddies and superstructures; [35]). Previous studies have found both the small and large scales to be energized with increase in  $\beta$  as well as  $\overline{\beta}(x)$  [15,27,28]. Similarly, Tanarro *et al.* [28] have noted that an increase in  $\text{Re}_\tau$  increases the large-scale energy in APG TBL, similar to

TABLE I. Effects on the small-scale ( $\lambda_y \lesssim \lambda_{y,c}$ ) and large-scale ( $\lambda_y > \lambda_{y,c}$ ) energy in the outer region ( $z^+ = zU_\tau/\nu \gtrsim 100$ ) of an APG TBL on independently increasing the three concerned parameters. It should be noted that this summary is applicable only for moderate APG ( $\beta \lesssim 2$ ) and low-to-moderate  $\text{Re}_\tau$  ( $500 \lesssim \text{Re}_\tau \lesssim 3000$ ) ranges investigated in the cited sources. In the case of ZPG TBL, however, the analysis is based on  $3000 \lesssim \text{Re}_\tau \lesssim 20\,000$  [13].  $\lambda_{y,c}$  corresponds to a nominal spanwise wavelength cutoff to segregate small (fine dissipative and viscous scales) and large (inertia-dominated) scales.

		ZPG TBL		APG TBL	
		Parameter	Scale	Parameter	Scale
		$\text{Re}_\tau \uparrow$	$\text{Re}_\tau \uparrow$	$\beta \uparrow$	$\bar{\beta} \uparrow$
Small-scale energy	<b>Negligible</b> Hutchins <i>et al.</i> [13]	<b>Decreases?</b> <i>present hypothesis</i>	<b>Increases</b> Monty <i>et al.</i> [27] Bobke <i>et al.</i> [15]	<b>Increases</b> Tanarro <i>et al.</i> [28]	
Large-scale energy	<b>Increases</b> Hutchins <i>et al.</i> [13]	<b>Increases</b> Tanarro <i>et al.</i> [28]	<b>Increases</b> Monty <i>et al.</i> [27] Bobke <i>et al.</i> [15]	<b>Increases</b> Tanarro <i>et al.</i> [28]	

the behavior noted for ZPG TBL [13]. However, none of the previous studies have investigated the  $\text{Re}_\tau$  effects on the small-scale energy, leaving open an important question. It is important because small scales from the inner region are advected away from the wall under a moderate APG [28], substantially increasing their contribution to the turbulent kinetic energy in the outer region [8,16,22]. This preliminary analysis of Tanarro *et al.* [28], however, was based on low- $\text{Re}_\tau$  simulations over an airfoil, which also suggested a decreasing influence of the APG with increasing  $\text{Re}_\tau$ . This makes it imperative to understand the small-scale dependency on  $\text{Re}_\tau$ , especially from the perspective of developing robust scaling arguments for the outer region. A hypothesis that naturally follows from the above discussion is the reduction in small-scale energy with  $\text{Re}_\tau$ . However, the hypothesis is in contrast with the viscous-scaled energy of the small scales in ZPG TBLs, which is influenced very weakly by  $\text{Re}_\tau$  in the outer region ( $\sim \text{Re}_\tau^{-1/4}$  [25]), making it quasi- $\text{Re}_\tau$  invariant or negligible (Table I). This is the primary motivation of the present study, which investigates the  $\text{Re}_\tau$  effects on the small-scale energy in the outer region of an APG TBL to potentially answer the open question highlighted in Table I.

Understanding this effect on the small scales is also important from the perspective of quantifying measurement errors. As discussed, establishing and testing scaling arguments for an APG TBL would require high- $\text{Re}_\tau$  data, available typically through experiments [18,23,26]. These measurements are conducted either using multicomponent anemometry [26,36,37], particle image velocimetry [7,18,38], or laser-Doppler velocimetry [39,40]. However, data from all of these measurement techniques inevitably suffer from spatial-resolution issues, leading to attenuated estimates of the small-scale energy [13,41]. This spatial-resolution issue, which is typically known to bring inaccuracies in the near-wall region, can, however, also adversely affect measurements in the outer region of an APG TBL, where small scales are statistically significant (at least at low  $\text{Re}_\tau$ ). This can be detrimental to high- $\text{Re}_\tau$  testing of scaling arguments, proposed based on low- $\text{Re}_\tau$  data (or vice versa). Although there are certain correction schemes to account for the spatial-resolution issues [42–45], they depend on direct numerical simulation (DNS) data sets or concepts based on canonical wall-bounded flows, which are not applicable for APG TBLs [30,37].

To this end, the present study investigates moderate APG TBLs on a smooth flat wall across  $600 \lesssim \text{Re}_\tau \lesssim 7000$ . It uses the published, well-resolved large-eddy simulation (LES) data set of Pozuelo *et al.* [8] across  $600 \lesssim \text{Re}_\tau \lesssim 2000$ , and a new experimental APG TBL data set from the large Melbourne wind tunnel, at  $\text{Re}_\tau \sim 7000$ . Both data sets correspond nominally to the same  $\beta$  range,  $1 \lesssim \beta \lesssim 2$ , thereby permitting analysis across a decade of  $\text{Re}_\tau$ . The present investigation is conducted through two approaches—spectral decomposition methodologies (Sec. IV) as well as

estimating velocity statistics for different numerical and experimental spatial resolutions (Sec. V). Consistent conclusions are obtained from both approaches, which confirms that our results are not a function of the sharp spectral cutoff ( $\lambda_{y,c}$ ) used for the first approach. Throughout this paper, fluid properties with superscript “+” represent normalization by viscous velocity ( $U_\tau$ ), length ( $\nu/U_\tau$ ), and time ( $\nu/U_\tau^2$ ) scales. Flow properties in capitals, or with overbars, represent mean spatial- or time-averaged properties, while those in lowercase represent fluctuations about their respective means. Cartesian coordinates  $x$ ,  $y$ , and  $z$  represent the streamwise, spanwise, and wall-normal directions, respectively, with  $u$ ,  $v$ , and  $w$  representing the associated velocity components.

## II. EXPERIMENTAL SETUP AND NUMERICAL DATABASE

This section gives details on the experimental and numerical data analyzed in the study. Both data sets are unique with regard to the manner in which the experiments and simulations were set up, enabling growth of an APG TBL with a well-defined upstream flow history.

### A. Experimental setup

Experiments were conducted in the open-circuit, large Melbourne wind tunnel at the University of Melbourne. Its test section has a cross section of  $\simeq 1.89 \times 0.92 \text{ m}^2$  and a long working section length of 27 m, which permits development of a thick turbulent boundary layer ( $\gtrsim 0.3 \text{ m}$ ) towards its downstream end. This aspect, combined with the ability to have free-stream speeds up to  $\sim 40 \text{ ms}^{-1}$ , enables investigation of high- $\text{Re}_\tau$  TBLs in this facility. Prior to this study, the wind tunnel was predominantly used for ZPG TBL research, and details regarding characterization of the associated setup can be found in Marusic *et al.* [46]. In this facility, a ZPG TBL is set up by installing a high-porosity screen (mesh) at the test-section outlet, which builds up a nominal back pressure in the test section. The ceiling of the test section comprises multiple air bleeds, spanning across the tunnel width and distributed at regular intervals along  $x$  [ $\sim 1.2 \text{ m}$ ; Fig. 1(a)], which allow excess air to escape owing to pressure build up. At the same time, it also removes the TBL developing on the ceiling. Such an arrangement establishes a controlled ZPG across the entire test-section length [46]. In the present paper, the high-porosity screen used for the ZPG TBL is henceforth referred to as the screen no. 0 configuration, which acts as the base configuration for all the APG experiments.

Setting up an APG TBL at high  $\text{Re}_\tau$ , with minimum upstream-history effects, demands unique modifications to the test section. The present study adopts the methodology used in the pioneering study of Clauser [4], where a gradual streamwise increment in the test-section static pressure was achieved by introducing blockage at the outlet section. Figure 1(c) shows a photograph of an aluminium screen, having a low porosity of 51%, installed at the outlet of the tunnel test section as a blockage. The screen is held rigidly on an aluminium frame at the tunnel outlet, with capacity to hold as many as six screens in total. In the present study, we either fix 1, 2, or 3 of these low-porosity screens in the frame (referred henceforth as configuration no. 1, 2, or 3), to systematically increase the static pressure in the test section. In the upstream part of the test section, however, a nominal ZPG is maintained always by controlling the outflow from the air bleeds on the ceiling, up to  $x \lesssim 9 \text{ m}$  [indicated by red arrows in Fig. 1(a)]. This ensures that the APG TBL growing beyond  $x > 9 \text{ m}$  begins with a high- $\text{Re}_\tau$  “canonical” upstream condition, i.e., with negligible upstream-history effects. Dynamic pressure [ $\rho U_1^2(x)/2$ ] was measured at various streamwise locations using a Pitot tube attached to a  $(x, z)$  traverse [Fig. 1(a); Marusic *et al.* [46]] at  $z = 0.525 \text{ m}$  from the wall, which is always in the free stream of both the top- and bottom-wall boundary layers. The Pitot tube is connected to a 10 torr Baratron manometer and signal conditioner. Atmospheric pressure and temperature were also acquired during the experiment, which facilitate conversion of the dynamic pressure to free-stream speeds. The resulting pressure coefficient,  $C_p = 1 - [U_1(x)/U_1(x=0)]^2$ , where  $U_1(x)$  is the free-stream velocity at  $x$ , is obtained for different screen number configurations and is shown in Fig. 1(b). The plots confirm that a nominal ZPG condition was maintained for

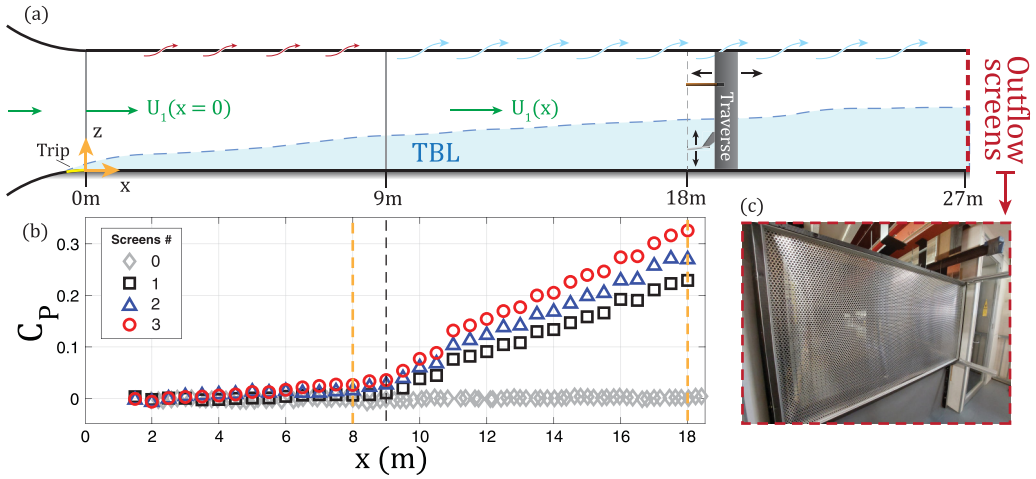


FIG. 1. (a) Schematic overview of the large Melbourne wind-tunnel test section modified to set up an APG TBL (not to scale). Markings in red indicate the modifications made for the APG setup, which include (i) controlling the air bleeding from the ceiling in the upstream section ( $x < 9$  m) to enforce a nominal ZPG, and (ii) introducing outflow screens at the test-section exit to increase tunnel static pressure. (b) Mean pressure coefficient,  $C_p$ , measured at various streamwise locations,  $x$ , for different screen no. configuration 0, 1, 2, or 3, with 0 corresponding to the scenario when ZPG is maintained across the entire tunnel test section. (c) Photograph of an aluminium outflow screen installed at the test-section outlet. The screen had circular holes of 9.5 mm diameter at a pitch of 12.7 mm, resulting in a porosity of 51%. Dashed gray line in (b) refers to the  $x$  location up to which a nominal ZPG was maintained, while dashed gold lines indicate locations for hotwire measurements.

$x < 9$  m, followed by a quasilinear growth in static pressure corresponding to the streamwise APG ( $x \gtrsim 9$  m).

Notably, the present setup adopted to impose streamwise pressure gradients is different from those adapted by past experimental studies [7,26,32,38–40], which predominantly relied on working section inserts (either on the ceiling or the “wall”) to establish the APG. Inclusion of working section inserts, however, introduces a constriction, which initially imposes a favorable pressure gradient, followed by a limited straight section for a ZPG, before finally leading to the APG region. Without due precaution, such setups can impose unique upstream histories that influence the scaling of the mean flow statistics of the APG flow [8,15]. To avoid these history effects, other studies have used an adjustable ceiling in the tunnel test section [9,14,26,27,32,36,40,47,48], the height of which is adjusted to decelerate the incoming flow and consequently generate a streamwise APG. Implementing this, however, requires a modular test section along with significant setup time, making it impractical for the large Melbourne wind tunnel.

All the data in Fig. 1(b) were obtained for free-stream conditions,  $U_1(x = 18 \text{ m}) \approx 10 \text{ ms}^{-1}$ . This matches the tunnel conditions for all (except one) new hotwire measurements presented in this study, which were conducted at  $x \approx 18$  m for screen no. 1, 2, or 3 configurations (i.e.,  $\beta > 0$ ; Table II). As highlighted in the table, these new hotwire measurements will be referred to as “Exp-APG” in the remainder of the paper, statistics from which will be compared with the published “Exp-ZPG” measurement ( $\beta = 0$ ) at nominally the same  $\text{Re}_\tau$ . Apart from these main measurements, another new hotwire measurement was conducted relatively upstream at  $x \approx 8$  m (with screen no. 3 configuration), i.e., towards the end of the controlled ZPG region, to demonstrate consistency with previously published ZPG TBL measurements at matched conditions (with screen no. 0 configuration; Table II). The consistency between these two measurements has been demonstrated in Appendix A and confirms the “canonical” upstream condition for the new Exp-APG experiments

TABLE II. Summary of the parameters associated with various hotwire measurements reported in this study. Definitions and terminologies have been provided in either Sec. I or II.  $Re_\theta$  is based on momentum thickness,  $\theta = \int_0^{\delta_{99}} [1 - U(z)/U_e][U(z)/U_e] dz$ . Numbers in bold correspond to hotwires with the best spatial resolution, and underlined numbers represent cases with matched experimental conditions  $x$ ,  $U_1$ ,  $\beta$ , and  $Re_\tau$  but different outflow screen configurations.

Ref.	Screens no.	$U_1(x=0)$ (m/s)	$x$ (m)	$U_1(x)$ (m/s)	$\beta(x)$	$Re_\tau$	$Re_\theta$	$U_\tau$ (m/s)	$\delta_{99}$ (m)	$\delta^*$ (mm)	$t^+$	$TU_1(x)/\delta_{99}$	$l^+$	Symbol	Source
-	0	<u>11.9</u>	<u>8</u>	<u>11.9</u>	0.0	4150	10 400	0.42	0.15	18	0.49	15 200	<b>22</b>	☆	Hutchins <i>et al.</i> [13]
-	3	<u>12.1</u>	<u>8</u>	<u>12</u>	0.0	4100	12 400	0.42	0.15	22	0.24	16 100	<b>14</b>	*	Present
Exp-ZPG	0	10.3	21	10.3	0.0	5600	19 400	0.33	0.27	38	0.34	17 400	<b>11</b>	◇	Hutchins <i>et al.</i> [13]
Exp-APG	1	11.3	18	10.0	0.9	6500	27 400	0.31	0.33	61	0.15	21 700	<b>10, 60</b>	□	Present
Exp-APG	2	11.7	18	10.0	1.3	6750	30 800	0.30	0.35	69	0.15	20 400	<b>10, 60</b>	△	Present
Exp-APG	3	12.1	18	10.0	1.7	6900	31 500	0.29	0.37	73	0.15	19 800	<b>10, 20, 40, 60</b>	○	Present



presented here. The hotwire measurements across the entire TBL were also made possible via the built-in traverse system, which has a Renishaw optical encoder (resolution  $\sim 0.1 \mu\text{m}$ ) to precisely record the relative wall-normal movement of the sensor. Velocity statistics reported here were acquired across the  $z$  range:  $0.5 \text{ mm} \lesssim z \lesssim 0.525 \text{ m}$ , at logarithmically spaced locations. In addition to these full TBL profiles, hotwires of the best spatial resolution (highlighted in bold in Table II) were also used to measure mean streamwise velocity very close to the wall, in and above the viscous sublayer ( $0.2 \text{ mm} < z \lesssim 0.5 \text{ mm}$ , i.e.,  $3 < z^+ \lesssim 8$ ). Such a measurement was possible at these high- $\text{Re}_\tau$  owing to the physically thick TBL and reasonably large viscous length scale in the Melbourne wind tunnel. The near-wall positioning of the hotwires, at the start of the measurement, was undertaken by using a traveling microscope (to measure near-wall distance) and a multimeter (to track conduction effects to wall), with the latter limiting its location to  $\gtrsim 0.2 \text{ mm}$  above the wall.  $U(z)$  measured in the viscous sublayer was used to estimate mean skin-friction velocity ( $U_\tau$ ) for both the Exp-ZPG and Exp-APG measurements, by forcing the measurements to fit over viscous-scaled mean velocity profiles ( $U^+ = U/U_\tau$ ) from published data sets [Figs. 3(a) and 3(c)]. We note here that while there are uncertainties associated with this method of estimating  $U_\tau$ , the key conclusions from the Exp-APG data set (Sec. V) are not dependent on the estimation method for  $U_\tau$ .

For the present study, the hotwire sensors were made in house using Wollaston wire, soldered onto Dantec 55P05 or 55P15 probes depending on the diameter ( $d$ ) and length ( $l$ ) of the platinum sensors. This capability made it possible to conduct experiments with systematically varying spatial resolution ( $10 \lesssim l^+ = lU_\tau/\nu \lesssim 60$ ) of the sensors. Hotwire sensors of various lengths ( $l = 0.5, 1, 2, \text{ and } 3 \text{ mm}$ ) were fabricated by carefully etching the Wollaston wire with nitric acid [49], to expose the platinum sensor. The sensors were made out of wires of either  $d = 2.5 \mu\text{m}$  or  $5 \mu\text{m}$  to maintain the aspect ratio,  $l/d \gtrsim 200$ , to avoid end-conduction effects [13]. The measurements were made using an in-house Melbourne University Constant Temperature Anemometer (MUCTA), at an overheat ratio of 1.8. Hotwire data were sampled during measurement at a frequency rate ( $f_s$ ), and for total acquisition time ( $T$ ), that satisfy  $t^+ = U_\tau^2/(f_s\nu) < 3$  and  $TU_1(x)/\delta_{99} > 20000$ , to have good temporal resolution and achieve statistical convergence, respectively [13]. Since it was challenging to maintain steady free-stream speeds below  $4 \text{ ms}^{-1}$  in the wind-tunnel test section, the hotwire calibration was conducted using two different arrangements, both in an *in situ* manner. A low-speed calibration was conducted using an in-house jet calibrator ( $0\text{--}5 \text{ ms}^{-1}$ ; [50]) and 0.1 torr Baratron manometer, which enables precise control across this low-speed range. Tunnel free-stream speeds ( $4\text{--}12 \text{ ms}^{-1}$ ) were used to calibrate the sensor across this higher speed range by maintaining the sensor at the same ( $x, z$ ) location, as the Pitot tube acquiring the reference free-stream speed. Pre- and postcalibrations were performed for all hotwire measurements, in conjunction with the “intermediate single point recalibration” (ISPR [51]) method of traversing the hotwires to the free stream, to correct for the hotwire sensor drift over the duration of measurement. Finally, all the sampled data was low-pass filtered at half the sampling frequency to avoid aliasing and high-frequency noise. All new measurements reported in this study (Table II) were conducted at least twice to confirm repeatability.

The key TBL characteristics ( $\beta, \text{Re}_\tau$ ) associated with all the hotwire experiments are documented in Table II and plotted in Fig. 2. These values have been reported based on the measurements conducted using hotwires with the best spatial resolution ( $l^+ \sim 10$ ). It should be noted that  $\text{Re}_\tau$  in this study is estimated based on  $\delta_{99}$ , which was obtained via the diagnostic-plot method recommended by Vinuesa *et al.* [3], for an APG TBL. Accordingly, the  $\text{Re}_\tau$  values associated with the measurements adopted from Hutchins *et al.* [13] have been recomputed based on the present definition. Quantification of the Clauser pressure-gradient parameter ( $\beta$ ) was made possible by combination of three different measurements: streamwise variation of test section pressure to estimate  $dP/dx$  (Pitot tube), velocity profile across the TBL to compute  $\delta^*$  (hotwire), and near-wall measurements to estimate  $U_\tau$  (hotwire), where  $dP/dx$  was estimated based on a linear fit for  $x > 9 \text{ m}$ , in Fig. 1(b). Since estimation of  $\bar{\beta}(x)$  is challenging in the case of experiments, quantifying upstream history of the Exp-APG data set is beyond the scope of the present study.

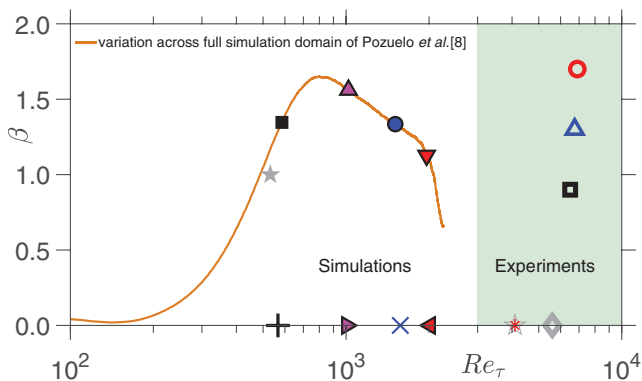


FIG. 2. Parameter space  $\beta$  vs  $Re_\tau$  using a combination of previously published data [8,13,15,52] and new experimental data. See Tables II and III for information on respective data sets.  $\beta$  vs  $Re_\tau$  is plotted across the full domain of the LES-APG data set [8] to indicate the upstream history for the selected locations (given by symbols).

### B. Numerical data set

The present study also considers previously published, well-resolved LES data of an APG TBL from Pozuelo *et al.* [8]. This APG database is unique as it has a long computational domain, a significant portion of which is maintained at a nominally constant  $\beta$ , i.e., at near-equilibrium condition. This makes it one of the ideal data sets to investigate  $Re_\tau$  effects on an APG TBL, especially also considering its broad  $Re_\tau$  range. For the purposes of referencing, this data set will be referred to as the “LES-APG” data set in the remainder of this paper. Figure 2 shows the variation of  $\beta$  with  $Re_\tau$  across the full numerical domain, which is compared against the parameters associated with the present experiments (Table II). Here we also compare and contrast the observations from LES-APG with a well-resolved LES data set of a ZPG TBL (henceforth referred as “LES-ZPG” [52]), which is available for the matched  $Re_\tau$  range as the LES-APG. For comparison, velocity statistics are extracted at four locations of the computational domain for both LES-APG and LES-ZPG, flow parameters for which have been highlighted with respective symbols in Fig. 2. In the case of LES-APG, the three locations at the highest  $Re_\tau$  are associated with the near constant  $\beta$  domain, while the lowest- $Re_\tau$  location is at similar  $\beta$  range but upstream of the constant  $\beta$  domain. Key TBL characteristics associated with these data sets are presented in Table III, with  $\Delta y^+$  numbers in bold representing the original grid resolution of the data sets in the spanwise direction. In order to investigate the influence of spatial resolution using the numerical data sets, the velocity time-series data saved at the four  $x$  locations was box filtered [43] across multiple grid points along the span, to estimate statistics for  $6 \lesssim \Delta y^+ \lesssim 69$ , consistent with  $10 \lesssim l^+ \lesssim 60$  range for the hotwires (Table II).

In Table III the numerical displacement thickness  $\delta_0^*$  refers to the displacement thickness of the laminar Blasius boundary layer imposed at the start of the numerical domain. Notably, all data locations considered for the present analysis are sufficiently far from the start of the computational domain ( $x/\delta_0^* \gtrsim 1500$ ). Another important aspect to note in the LES-APG case is the steep increment in  $\beta$ , upstream of the nominally constant  $\beta$  region, which is in contrast with the nominal ZPG condition maintained in case of Exp-APG data set [Fig. 1(b)]. Hence, the statistics from LES-APG are inevitably influenced by the upstream-history effects. This has been quantified by computing  $\bar{\beta}(x)$ , which indicates stronger history effects with increasing  $x$  locations (i.e., increasing  $Re_\tau$ ). As discussed, based on Table I, stronger history effects are known to increase small-scale energy in the APG TBLs. This has also been demonstrated in Appendix D by comparing statistics from LES-APG, with the data set of Bobke *et al.* [15], for similar  $\beta$  and  $Re_\tau$  but varying  $\beta$  (refer to



TABLE III. Summary of the parameters associated with various numerical databases analyzed in this study. Definitions and terminologies have been provided in either Sec. I or II.  $\Delta y^+$  corresponds to the various spanwise grid resolutions used to estimate the velocity statistics, with the numbers in bold corresponding to the original, well-resolved grid of the data set. Underlined numbers represent cases with reasonably similar  $\beta$  and  $\text{Re}_\tau$  but different upstream history,  $\bar{\beta}(x)$ .

Ref.	$x/\delta_o^*$	$\beta(x)$	$\bar{\beta}(x)$	$\text{Re}_\tau$	$\text{Re}_\theta$	$\Delta y^+$	Symbol	Source
LES-ZPG	1500	0	0	566	1638	<b>13</b>	+	Eitel-Amor <i>et al.</i> [52]
LES-ZPG	3500	0	0	1007	3136	<b>12</b>	▶	Eitel-Amor <i>et al.</i> [52]
LES-ZPG	6500	0	0	1572	5115	<b>12</b>	×	Eitel-Amor <i>et al.</i> [52]
LES-ZPG	9000	0	0	2017	6657	<b>12</b>	◀	Eitel-Amor <i>et al.</i> [52]
–	1277	<u>1.0</u>	0.84	<u>531</u>	2153	<b>8</b>	★	Bobke <i>et al.</i> [15]
LES-APG	1500	<u>1.3</u>	0.67	<u>585</u>	2362	<b>11, 21, 43, 64</b>	■	Pozuelo <i>et al.</i> [8]
LES-APG	3500	1.6	1.17	1020	4915	<b>8, 23, 38, 69</b>	▲	Pozuelo <i>et al.</i> [8]
LES-APG	6000	1.3	1.26	1508	7160	<b>7, 20, 40, 67</b>	●	Pozuelo <i>et al.</i> [8]
LES-APG	8500	1.1	1.26	1959	8959	<b>6, 19, 44, 63</b>	▼	Pozuelo <i>et al.</i> [8]

Table III). The trend of increasing small-scale energy with  $\bar{\beta}$ , however, is not noted while comparing small-scale statistics at increasing  $\text{Re}_\tau$  (Sec. IV), suggesting history effects are weak and will not influence our conclusions associated with  $\text{Re}_\tau$  effects, drawn from the LES-APG data set. Indeed,  $\bar{\beta}(x = 6000\delta_o^*) \approx \bar{\beta}(x = 8500\delta_o^*)$ , reinforcing that history effects are weak towards the end of the computational domain. Readers are referred to the respective articles [8,52] for further details on the numerical method, computational grid ( $\Delta x^+$ ,  $\Delta z^+$ ), etc., associated with the LES-ZPG and LES-APG data sets, respectively.

### III. EXPERIMENTAL DATA AT HIGH REYNOLDS NUMBERS

This section presents the high- $\text{Re}_\tau$  ( $\sim 6000$ – $7000$ ) Exp-APG data set, measured with the best available hotwire spatial resolution ( $l^+ \approx 10$ ; Table II), and compares it with previously published data. Specifically, the mean velocity profiles, streamwise normal stresses, and energy spectrograms for  $u$  fluctuations are compared for Exp-ZPG and Exp-APG data sets. The idea is to demonstrate their consistency with trends noted previously in the literature [26,27,30,39] for varying  $\beta$  in the low-to-moderate APG range ( $0 \lesssim \beta \lesssim 2$ ).

Figure 3(a) compares the viscous-scaled mean streamwise velocity ( $U^+$ ) from Exp-APG and Exp-ZPG and compares it with published simulation data sets at low  $\text{Re}_\tau$ , but in a similar  $\beta$  range. Consistent with the findings of Nickels [54], we note that the simulation data collapse for  $z^+ < 10$ , which is made clearer by the enlarged plot shown in Fig. 3(c). Similar collapse of the near-wall  $U^+$  profiles for ZPG and APG TBL (with moderate  $\beta$ ) was also noted by Krogstad and Skåre [55] and Monty *et al.* [27], thereby forming a strong basis to estimate  $U_\tau$  for the present experiments. To this end, the mean velocity recorded from the near-wall hotwire measurements ( $0.2 \text{ mm} \lesssim z \lesssim 0.5 \text{ mm}$ ), conducted for various  $\beta$ , are forced to fit over the published data as depicted in Fig. 3(c). This fit is used to estimate  $U_\tau$  for the Exp-ZPG and Exp-APG data sets presented in Fig. 3, which is recorded in Table II. Notably,  $U_\tau$  estimated for Exp-ZPG case matches well with the  $U_\tau$  reported by Hutchins *et al.* [13], reinforcing confidence in the methodology.

In the wake region [Fig. 3(e)],  $U^+$  can be noted to increase in a way that suggests increasing size of the wake region with increasing  $\beta$ , which is expected [9,27]. Next, we shift our focus to the intermediate  $z^+$  range,  $O(10^2) < z^+ < O(10^3)$ , where one could argue a logarithmic variation of  $U^+$  vs  $z^+$  (i.e., the log law). This region, which is enlarged in Fig. 3(d) for clarity, suggests a systematic deviation of  $U^+$  from the log law as  $\beta$  increases. This observation is consistent with the findings of Monty *et al.* [27], who also investigated  $U^+$  vs  $z^+$  trends for varying  $\beta$  at matched  $\text{Re}_\tau$ .

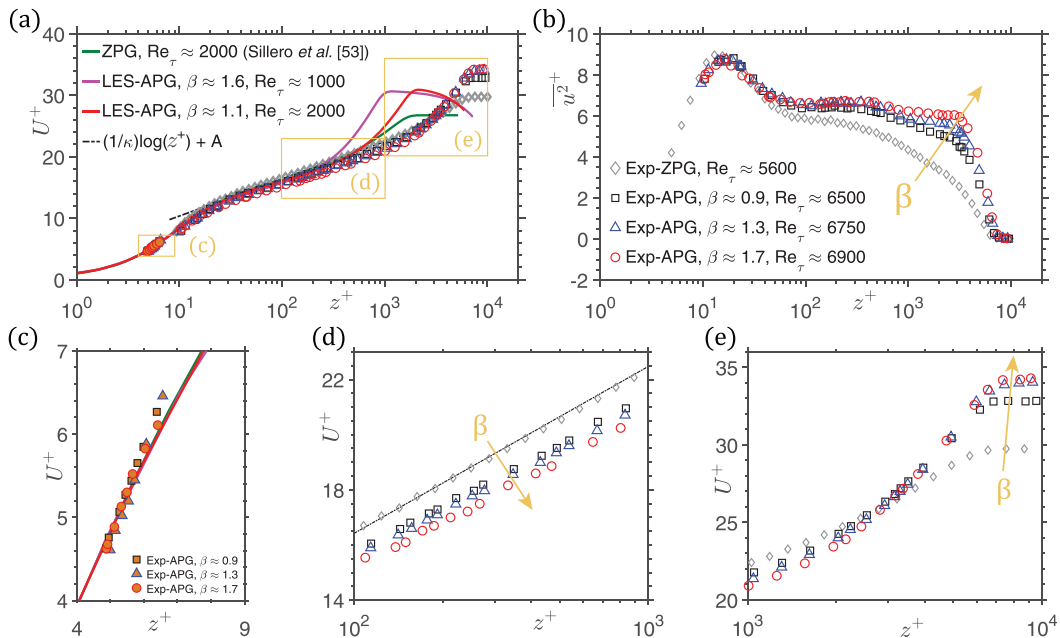


FIG. 3. Viscous-scaled (a), (c), (d), (e) mean velocity profiles and (b) streamwise normal stresses corresponding to the Exp-ZPG and Exp-APG data sets with  $l^+ \approx 10$  (Table II). In (a), the high- $Re_\tau$  experimental data are compared with low- $Re_\tau$  ZPG TBL data set of Sillero *et al.* [53] and the well-resolved LES-APG data set (Table III). Panels (c)–(e) depict the enlarged views of data in specific  $z^+$  ranges in (a), indicated by yellow boxes. Solid lines correspond to complete velocity profiles from simulation data sets, and open symbols correspond to experimental data acquired across the TBL. Filled symbols in (a) and (c) are from the dedicated experiments conducted very close to the wall to estimate skin-friction velocity,  $U_\tau$ . Dash-dotted black line in (a) and (d) corresponds to the well-known log law of the mean velocity following Marusic *et al.* [6], with  $\kappa = 0.39$  and  $A = 4.3$ .

Definitively determining whether this deviation is due to decreases in the value of the slope  $\kappa$  [7] and/or a change in intercept “A,” would require further careful investigation, while also accounting for the measurement uncertainty, and hence is out of scope (and focus) of the present study. Moving to Fig. 3(b), the trends associated with  $\overline{u^2}^+$  profiles obtained from Exp-ZPG and Exp-APG are also consistent with the literature [27,30]. Energy in the outer region can be noted to increase significantly with  $\beta$ , with the  $\overline{u^2}^+$  profile tending to plateau in the outer region for the largest  $\beta \approx 1.7$ . The fact that no distinct outer peak can be noted in Fig. 3(b) is not surprising, and the plateauing of the  $\overline{u^2}^+$  profile in this  $\beta$  range is consistent with the previous experimental studies at  $Re_\tau \gtrsim O(10^3)$  [26,27,30,39], which noted a distinct outer peak only for  $\beta \gtrsim 2$ . Streamwise normal stresses in the inner region, on the other hand, do not appear to change significantly in the  $\beta$  and  $Re_\tau$  range considered, which is also consistent with the studies of Aubertine and Eaton [39] and Romero *et al.* [26].

In order to appreciate which turbulent scales contribute to the growth of  $\overline{u^2}^+$  in the outer region, Fig. 4 shows the  $u$  spectrograms as a function of  $z^+$  and  $\lambda_\tau^+$  for the Exp-ZPG and Exp-APG data sets considered in Fig. 3. Following Harun *et al.* [14] and Sanmiguel Vila *et al.* [30], here we use Taylor’s frozen turbulence hypothesis to convert time series to spatial length scales. For this, we use the mean streamwise velocity at each  $z^+$  as the mean convection velocity of all the turbulent scales coexisting at  $z^+$ . In general, variation in the scale-based energy distribution in the outer region, with  $\beta$ , is very similar to that noted previously by Sanmiguel Vila *et al.* [30] (refer to their Fig. 3).

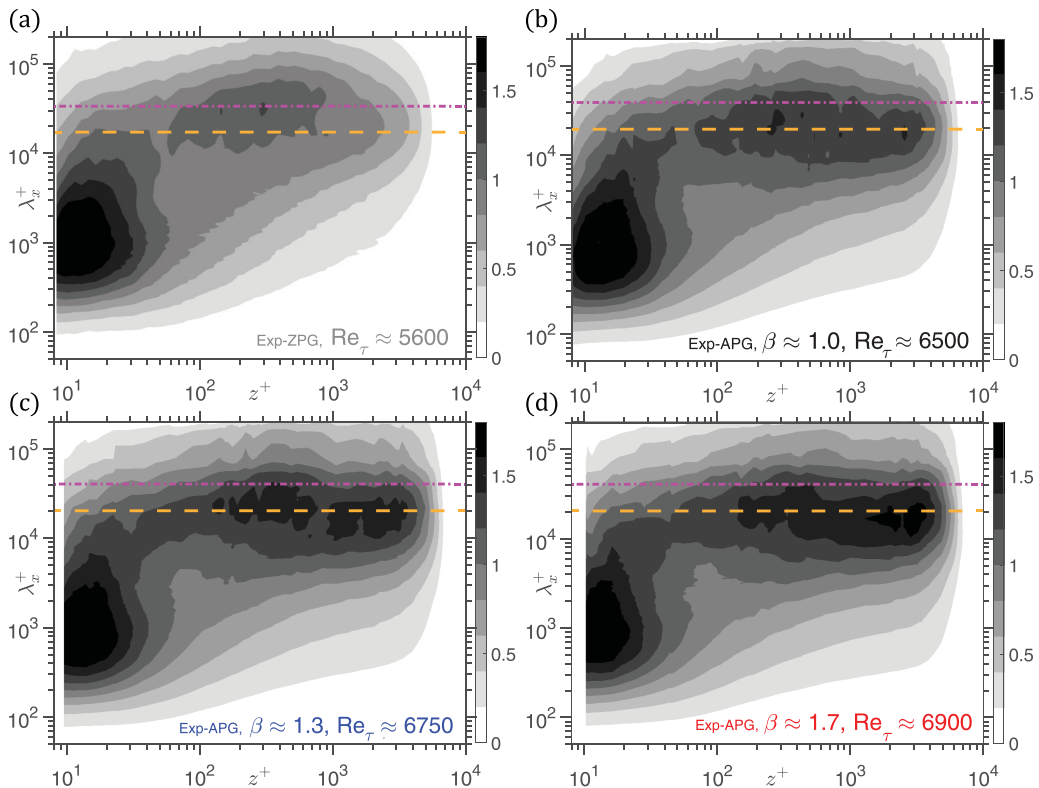


FIG. 4. Viscous-scaled premultiplied energy spectra of the streamwise velocity fluctuations ( $k_x \phi_{uu}^+$ ), as a function of  $\lambda_x^+$  and  $z^+$ , computed from the Exp-ZPG and Exp-APG data sets with  $l^+ \approx 10$  (Table II). Dashed yellow and dash-dotted magenta lines indicate  $\lambda_x^+ = 3\delta_{99}^+$  and  $\lambda_x^+ = 6\delta_{99}^+$ , respectively.

For the Exp-ZPG data [Fig. 4(a)], a characteristic outer peak can be noted at  $\lambda_x^+ \sim 6\delta_{99}^+$  in the log region [13]. However, as  $\beta$  increases to 0.9, scales coexisting beyond  $z^+ > 10^3$  get significantly more energetic than in Exp-ZPG, with energy concentrating at  $\lambda_x^+ \sim 3\delta_{99}^+$  in this region. This energy enhancement exists alongside the energy concentration noted at  $\lambda_x^+ \sim 6\delta_{99}^+$ , the same as in Exp-ZPG. As  $\beta$  is increased further to 1.3 and 1.7, energy increases near both,  $\lambda_x^+ \sim 3\delta_{99}^+$  and  $\sim 6\delta_{99}^+$ , consistent with Harun *et al.* [14] and Sanmiguel Vila *et al.* [30]. Hence, based on Figs. 3 and 4, we can conclude that the new Exp-APG data set provides trends consistent with those in the literature, with larger values of  $\beta$  increasing energy predominantly in the large scales. This paves the way to use this data set, with additional measurements at varying spatial resolution  $l^+$ , for further analysis in Sec. V.

#### IV. REYNOLDS-NUMBER EFFECT ON THE OUTER REGION OF APG TBL

After establishing and discussing the quality of the Exp-APG data set, we now compare and contrast it with the numerical data sets (LES-ZPG and LES-APG) to bring out the  $Re_\tau$  trends associated with the streamwise normal stresses. For this, we begin by comparing  $\overline{u^{2^+}}$  and the corresponding energy spectra in Fig. 5. The  $Re_\tau$  trend observed for  $\overline{u^{2^+}}$  of a canonical wall-bounded flow [Fig. 5(a)] is already well established in the literature [13,56]. It involves a modest increase in energy of the inner peak, located at  $z^+ \approx 15$ , and a significant growth of the outer region across  $600 \lesssim Re_\tau \lesssim 6000$ . In the case of LES-APG, however, the variation of  $\overline{u^{2^+}}$  in the outer region, for a similar  $Re_\tau$  range, is indeterminate [Fig. 5(b)]. A significant increase in the outer region,

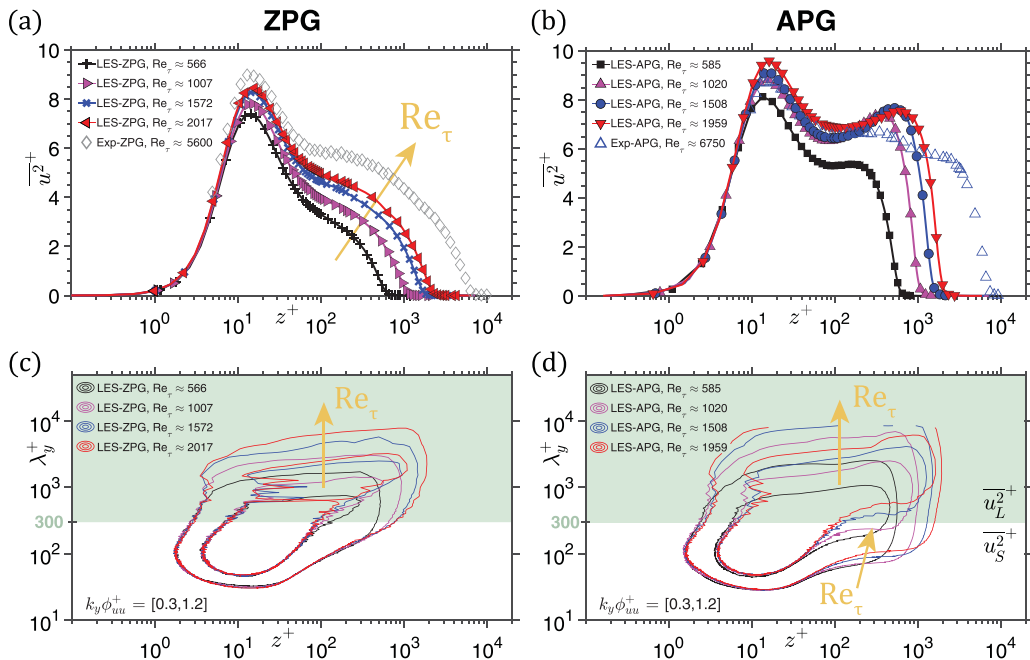


FIG. 5. (a), (b) Streamwise normal stress,  $\overline{u^2}^+$  and (c), (d) constant energy contours of premultiplied  $u$  spectra for (a), (c) ZPG TBL and (b), (d) APG TBL data sets at various  $Re_\tau$ . Estimates for LES-ZPG and LES-APG data sets correspond to their original (i.e., well-resolved) grid resolution ( $\Delta y^+$ ; Table III), while those for Exp-ZPG and Exp-APG are from hotwires with  $l^+ \approx 10$  (Table II). Symbols and color scheme for each data set are as documented in Sec. II. White and green background in (c) and (d) indicate small-scale ( $\overline{u_S^2}^+$ ;  $\lambda_y^+ \leq 300$ ) and large-scale contributions ( $\overline{u_L^2}^+$ ;  $\lambda_y^+ > 300$ ), respectively.

with emergence of an outer peak, can be noted as  $Re_\tau$  increases from 585 to 1020. However, this growth seems to stagnate with further increase in  $Re_\tau$  across  $1000 \lesssim Re_\tau \lesssim 2000$ . For the purpose of comparison, Fig. 5(b) also includes  $\overline{u^2}^+$  profile obtained from the best-resolved hotwires ( $l^+ \sim 10$  for  $\beta \sim 1.3$  and  $Re_\tau \approx 6750$ ). While it is not appropriate to make a quantitative comparison between the LES-APG and Exp-APG cases owing to their different upstream histories, the high- $Re_\tau$  Exp-APG data do indicate that the indeterminate trend associated with  $\overline{u^2}^+$  is not due to the relatively narrow  $Re_\tau$  range of the LES-APG study. The Exp-APG data also conform to similar  $\overline{u^2}^+$  levels in the outer region as LES-APG, which is in contrast with the trend noted from LES-ZPG and Exp-ZPG in the same  $Re_\tau$  range.

To further examine the different trends for  $\overline{u^2}^+$  in the outer region of APG and ZPG TBLs, we consider the constant-energy contours of  $u$ -energy spectra from LES-ZPG and LES-APG in Figs. 5(c) and 5(d), respectively. Here we did not consider spectra from Exp-ZPG and Exp-APG data sets owing to unavailability of energy distributions as a function of  $\lambda_y$ . In the case of LES-ZPG, the constant-energy contours exhibit a convincing collapse for the  $u$  spectra in the small-scale range across  $600 \lesssim Re_\tau \lesssim 2000$ . Furthermore, energy in the large scales can be noted to increase with  $Re_\tau$  [13], as indicated by the outward shift of the contours towards higher  $\lambda_y^+$ . As for the energy contours from LES-APG, the large-scale energy can again be noted to increase with  $Re_\tau$  [28]. However, a contrasting trend is noted for the relatively small scales, where contours are noted to shift inwards, indicating a decrease in energy with  $Re_\tau$ .

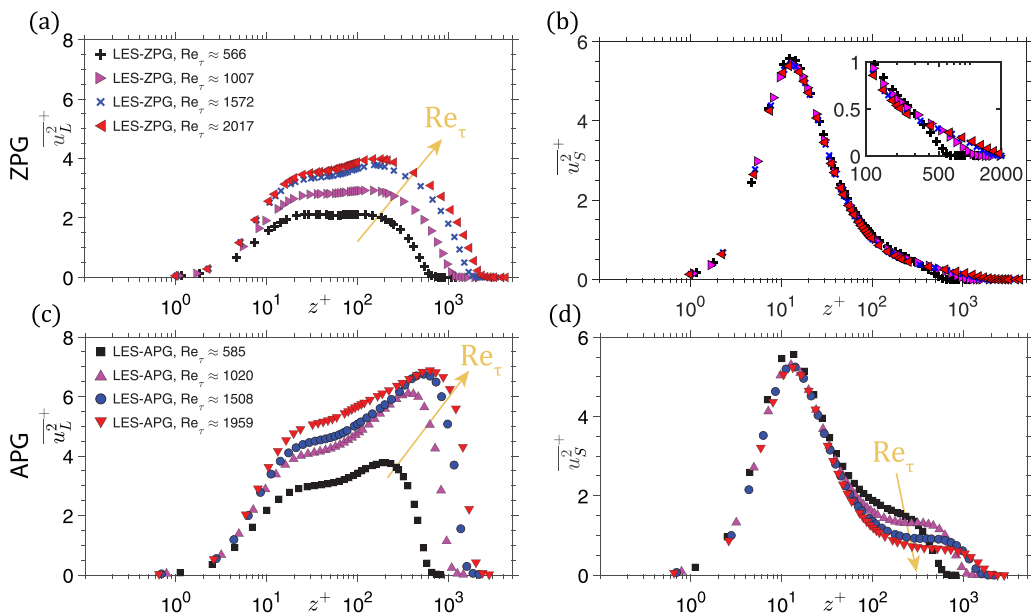


FIG. 6. Streamwise normal stress decomposed into viscous-scaled (a), (c) large-scale ( $\overline{u_L^2}^+$ ) and (b), (d) small-scale contributions ( $\overline{u_S^2}^+$ ) for (a), (b) LES-ZPG and (c), (d) LES-APG data sets at various  $Re_\tau$ . Estimates for the simulation data sets correspond to their original (i.e., well-resolved) grid resolution ( $\Delta y^+$ ; Table III).

To clearly bring out the  $Re_\tau$  trends of the small- and large-scale energy from LES-ZPG and LES-APG, we consider decomposing the total streamwise variance ( $\overline{u^2}^+$ ) into its large ( $\overline{u_L^2}^+$ ) and small ( $\overline{u_S^2}^+$ ) energy contributions. To this end we use a sharp spectral cutoff at  $\lambda_{y,c}^+ = 300$  to decompose  $\overline{u^2}^+ = \overline{u_S^2}^+ + \overline{u_L^2}^+$ . Here a constant viscous-scaled cutoff has been chosen based on a careful consideration of published data sets of canonical wall-bounded flows [52,53,56,57], to segregate a fixed range of small (viscous) scales. The  $\overline{u_S^2}^+$  distributions obtained from these data sets exhibited a quasi- $Re_\tau$  invariance [13] for  $\lambda_{y,c}^+ \lesssim 300$ , a fact that was used as a basis to select  $\lambda_{y,c}^+ = 300$  [57]. This has been demonstrated for the DNS data set of turbulent channel flow [56] in Appendix C, as well as for the LES-ZPG data set in Fig. 6(b). It is, however, important to note that the present conclusions do not depend on the exact choice of  $\lambda_{y,c}^+$ , which is used to simply reveal the contrasting trends in  $\overline{u_S^2}^+$  for LES-ZPG and LES-APG. Figure 6 shows  $\overline{u_L^2}^+$  and  $\overline{u_S^2}^+$  obtained using  $\lambda_{y,c}^+ = 300$  for LES-ZPG and LES-APG data sets. These plots now clearly show the trends discussed based on the spectra in Figs. 5(c) and 5(d):  $\overline{u_L^2}^+$  can be noted to increase across the entire TBL for both LES-APG and LES-ZPG, and is representative of the increase in energy of the inertial scales with increasing  $Re_\tau$  (i.e., Townsend's attached eddies and superstructures [35]). While  $\overline{u_S^2}^+$  is quasi- $Re_\tau$  invariant for LES-ZPG across entire TBL, and in the near-wall region for LES-APG, which would be expected for the fine dissipative and viscous scales associated with this small-scale range [13]. The inset in Fig. 6(b) confirms that the  $Re_\tau$  invariance of  $\overline{u_S^2}^+$  extends up to as high as  $z^+ \lesssim 0.8Re_\tau$ , beyond which  $\overline{u_S^2}^+$  gradually decreases to zero owing to the increasing influence of the turbulent-nonturbulent interface of the TBL. Interestingly, however,  $\overline{u_S^2}^+$  for the LES-APG can be noted to decrease with  $Re_\tau$  in the outer region, which is consistent with our hypothesis discussed

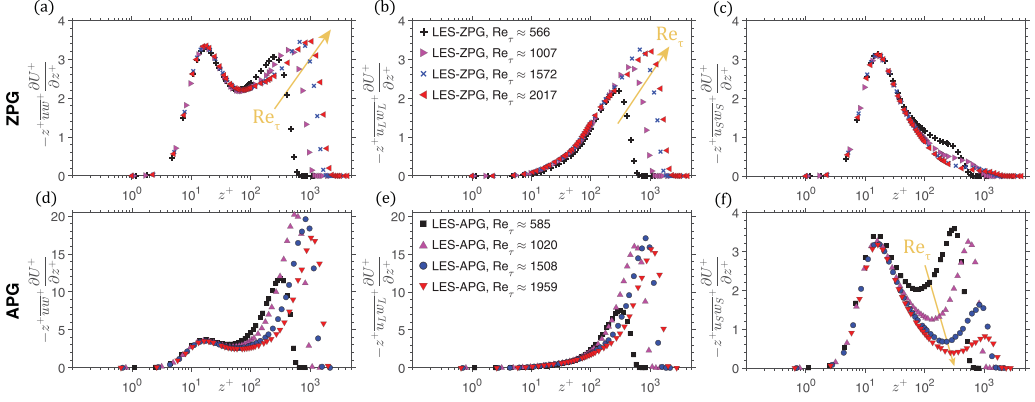


FIG. 7. (a), (d) Dominant contribution to production of turbulent-kinetic energy,  $-\overline{uw}^+ \partial U^+ / \partial z^+$ , decomposed into viscous-scaled (b), (e) large-scale ( $-\overline{u_L w_L}^+ \partial U^+ / \partial z^+$ ) and (c), (f) small-scale contributions ( $-\overline{u_S w_S}^+ \partial U^+ / \partial z^+$ ) for (a)–(c) LES-ZPG and (d)–(f) LES-APG data sets at various  $Re_\tau$ . Estimates for the simulation data sets correspond to their original grid resolution ( $\Delta y^+$ ; Table III). Note that the profiles are premultiplied with  $z^+$ . Also, the range of the vertical axis for (a), (b), (c), and (f) is different than for (d) and (e).

in Sec. I. The contrasting trends exhibited by  $\overline{u_L}^2$  and  $\overline{u_S}^2$  in the outer region for LES-APG explain the indeterminate variation of  $\overline{u}^2$ , with  $Re_\tau$ , in Fig. 5(b).

To understand the origins of the decrease in small-scale energy with  $Re_\tau$ , we consider the turbulent-kinetic-energy budget. Specifically, we investigate the production of the total turbulent-kinetic-energy,  $k^+ = (\overline{u}^2 + \overline{v}^2 + \overline{w}^2)/2$ , given by  $P_k^+ = -\overline{u_i u_j}^+ (\partial U_i^+ / \partial x_j^+)$  [8,15], where  $i$  and  $j$  represent the conventional tensor notations. In the case of APG TBLs,  $P_k^+ = -\overline{u}^2 (\partial U^+ / \partial x^+) - \overline{w}^2 (\partial W^+ / \partial z^+) - \overline{uw}^+ (\partial U^+ / \partial z^+ + \partial W^+ / \partial x^+)$ , out of which  $-\overline{uw}^+ (\partial U^+ / \partial z^+)$  has been found to be much larger than the other three terms [8,16], at least in the case of moderate  $\beta$ . Also note that  $-\overline{uw}^+ (\partial U^+ / \partial z^+)$  is also the only nonzero term when  $P_k^+$  is expanded for the case of canonical wall flows [57,58] and is essentially the product of the Reynolds shear stress ( $\overline{uw}^+$ ) and mean velocity gradient ( $\partial U^+ / \partial z^+$ ) at any  $z^+$ . Hence, we limit our attention to this term and analyze its variation with  $Re_\tau$  using LES-ZPG and LES-APG data sets. We also decompose  $-\overline{uw}^+ (\partial U^+ / \partial z^+)$  into dominant contributions from the small [ $-\overline{u_S w_S}^+ (\partial U^+ / \partial z^+)$ ] and large scales [ $-\overline{u_L w_L}^+ (\partial U^+ / \partial z^+)$ ] by using the same spectral cutoff ( $\lambda_{y,c}^+ = 300$ ) to segregate  $w = w_S + w_L$ .

Figure 7 shows these three terms in a premultiplied form following Marusic *et al.* [58], so that equal areas under the graph represent equal integral contributions. In the case of LES-ZPG, the  $Re_\tau$  trends are again consistent with the literature [57,58], where increasing  $Re_\tau$  increases the production of turbulent-kinetic energy in the outer region. This can be associated with increasing production in the large scales, while variation in the small-scale characteristics is negligible. In comparison to LES-ZPG, the production in the outer region of LES-APG is enhanced significantly, which is also well known in the literature [8,9,15,16]. However, it is evident from Fig. 7(d) that the outer peak in  $-\overline{uw}^+ (\partial U^+ / \partial z^+)$  appears to be reducing with  $Re_\tau$ , opposite to the trend for LES-ZPG. While this observation was discussed in Pozuelo *et al.* [8], here we can associate this decrease partly to the decrease in production of turbulence in the small scales with  $Re_\tau$ , represented by  $-\overline{u_S w_S}^+ (\partial U^+ / \partial z^+)$  in Fig. 7(f). This reduction in the turbulence production, thus, gives a physical explanation for the drop in  $\overline{u_S}^2$  with increasing  $Re_\tau$ , in Fig. 6(d). The fact that this decrease in  $\overline{u_S}^2$  and  $-\overline{u_S w_S}^+ (\partial U^+ / \partial z^+)$  in the outer region is purely a  $Re_\tau$  effect, and not an artifact of increasing  $\beta$  (Table III), has been confirmed in Appendix D. Similarly, we can argue that this decrease in



small-scale contributions is not an artifact of mild changes in  $\beta$ ; the argument is based on the fact that the trend is consistent despite the contrasting variations in  $\beta$  (Table III), which slightly increases for  $585 \lesssim \text{Re}_\tau \lesssim 1020$ , is equal for  $\text{Re}_\tau \sim 585$  and  $1508$ , after which it declines for  $\text{Re}_\tau \sim 1959$ . It is worth noting in the case of Fig. 7 that the spectral decomposition of  $-\overline{uw}^+(\partial U^+/\partial z^+)$  also leads to two other terms,  $-\overline{u_S w_L^+}(\partial U^+/\partial z^+)$  and  $-\overline{u_L w_S^+}(\partial U^+/\partial z^+)$ , which, however, are much smaller than the two main terms plotted in the figure (and are, hence, neglected).

## V. SPATIAL-RESOLUTION EFFECT FOR VARYING REYNOLDS NUMBER

The analysis presented in Sec. IV concludes that the turbulent-kinetic energy of the small scales, in the outer region of an APG TBL, reduces with increasing  $\text{Re}_\tau$ . This will have ramifications for the measurement errors arising due to spatial resolution issues, which we know are associated with attenuation of the small-scale energy contributions [13]. A decrease in small-scale energy with increasing  $\text{Re}_\tau$ , noted here for an APG TBL, should reduce the attenuation in  $\overline{u^2}^+$  profiles estimated for various spatial resolutions (with increasing  $\text{Re}_\tau$ ). This is tested in Fig. 8, which compares LES-APG  $\overline{u^2}^+$  profiles and the corresponding  $u$  spectra, estimated for various spatial resolutions ( $\Delta y^+$ ), as documented in Table III. The spatial resolution is systematically varied for each  $\text{Re}_\tau$  case in the range  $6 \lesssim \Delta y^+ \lesssim 69$ . Since our focus is on the outer region, the outer peak ( $z_{OP}^+$ ) associated with each LES-APG case is identified from well-resolved data and marked in Fig. 8 as a dashed line. It is evident from Fig. 8 that an increase in  $\Delta y^+$  attenuates the estimated normal stress,  $\overline{u^2}^+$ . However, the degree of attenuation varies across the TBL thickness as well as for each  $\text{Re}_\tau$ . To quantify this variation in attenuation for the outer region, we compute the difference in  $\overline{u^2}^+$  for the well-resolved and worst-resolved case at  $z_{OP}^+$  for each  $\text{Re}_\tau$ . This is defined as  $\Delta \overline{u^2}^+(z_{OP}^+)$  for each LES-APG case in Fig. 8 and plotted in Fig. 9 as a function of  $\text{Re}_\tau$ . It is evident that the energy attenuation [ $\Delta \overline{u^2}^+(z_{OP}^+)$ ] owing to increasing  $\Delta y^+$  is reduced with  $\text{Re}_\tau$ . The constant-energy contours of the  $u$  spectra, plotted in Figs. 8(b), 8(d), 8(f), and 8(h) for different  $\text{Re}_\tau$ , confirm that this energy attenuation occurs solely in the small-scale range ( $\lambda_y^+ \lesssim 300$ ), as expected. Hence, the spectra not only support the usage of  $\lambda_{y,c}^+ = 300$  for decomposing  $\overline{u^2}^+$  into  $\overline{u_L^2}^+$  and  $\overline{u_S^2}^+$ , but also indicate that the decreasing trend of  $\Delta \overline{u^2}^+(z_{OP}^+)$  with  $\text{Re}_\tau$  is solely associated with reduced attenuation of the small-scale energy with  $\text{Re}_\tau$ . This, in turn, is associated with the reduction in small-scale energy in the outer region with  $\text{Re}_\tau$  [Fig. 5(d)].

The trend associated with reduction of  $\Delta \overline{u^2}^+(z_{OP}^+)$  with increasing  $\text{Re}_\tau$  in Fig. 9 can be used to estimate approximate  $\text{Re}_\tau$  range when  $\Delta \overline{u^2}^+(z_{OP}^+) \rightarrow 0$ . The simplest way is to fit a straight line, which indicates  $\Delta \overline{u^2}^+(z_{OP}^+) \approx 0$  for  $\text{Re}_\tau \gtrsim 3000$ . It should be noted, however, that this is a very crude estimate based on a very limited parameter range ( $\beta, \bar{\beta}$ ) and is also specific to the spatial resolution associated with well-resolved ( $\Delta y^+ \sim 6$ ) and worst-resolved ( $\Delta y^+ \sim 69$ ) cases considered here. This prediction can be tested in the present study by using the high- $\text{Re}_\tau$  Exp-APG data set, acquired for a similar range of spatial resolution ( $10 \lesssim l^+ \lesssim 60$ ) and moderate  $\beta$  range as the LES-APG. Figure 10 depicts  $\overline{u^2}^+$  and constant-energy contours of the associated  $u$ -energy spectra from the Exp-APG data set for various  $\beta$  and spatial resolutions. Remarkably,  $\overline{u^2}^+$  can be noted to attenuate with increasing  $l^+$  only in the inner region ( $z^+ < 100$ ), with negligible changes in the outer region. Although there is no clear outer peak evident in  $\overline{u^2}^+$  for Exp-APG data, for the purpose of comparison, we estimate  $\Delta \overline{u^2}^+(z_{OP}^+)$  for these data by using  $z_{OP}^+ \sim 0.3\delta_{99}^+$  following Sanmiguel Vila *et al.* [30] and plot it in Fig. 9. Indeed,  $\Delta \overline{u^2}^+(z_{OP}^+) \sim 0$  at  $\text{Re}_\tau \gtrsim 6500$  associated with Exp-APG, consistent with the crude prediction from Fig. 9.

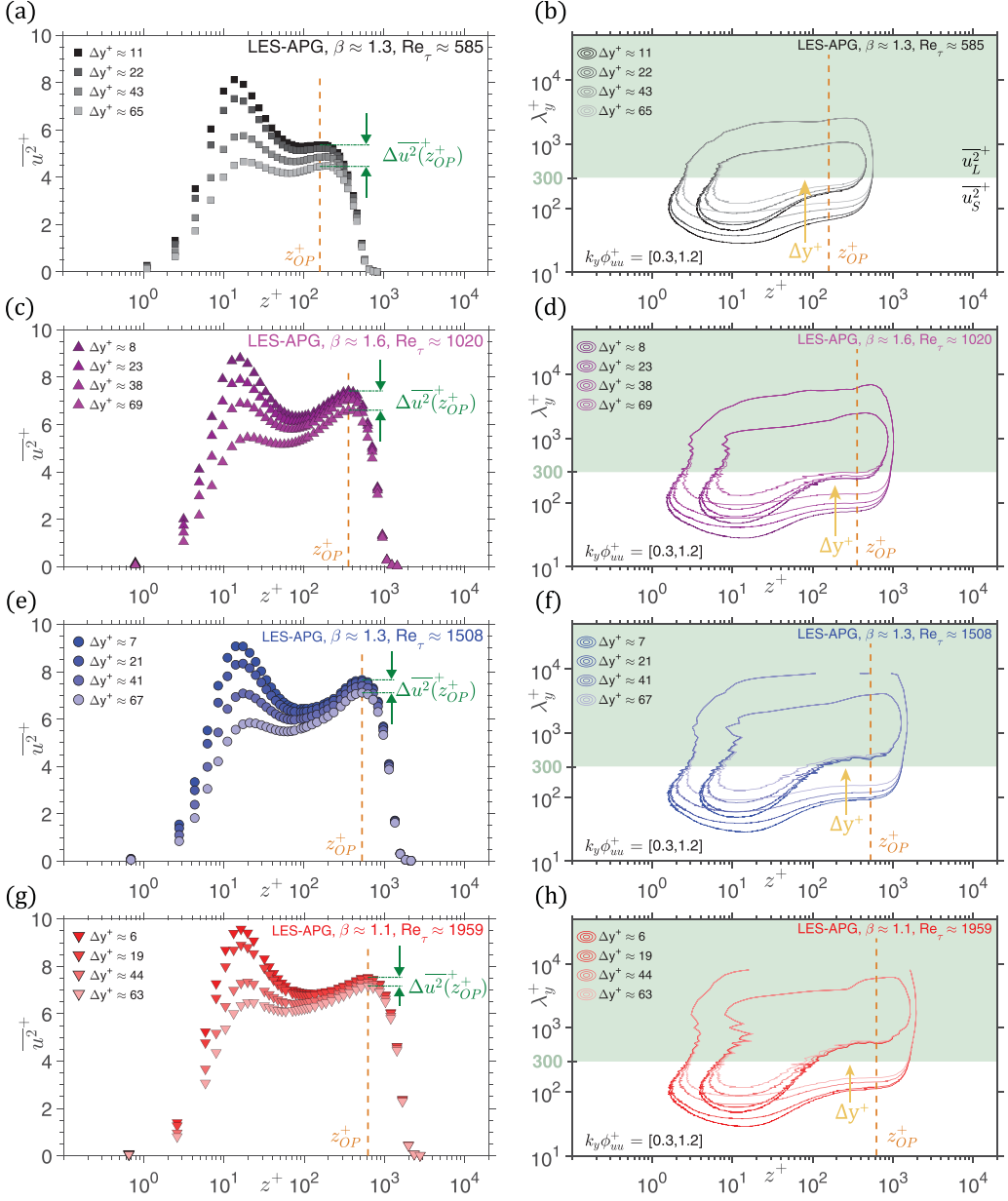


FIG. 8. (a), (c), (e), (g) Streamwise normal stress,  $\overline{u^2}^+$  and (b), (d), (f), (h) constant-energy contours of premultiplied  $u$  spectra estimated for LES-APG data sets with various spatial resolutions ( $\Delta y^+$ ) at  $\text{Re}_\tau \approx$  (a), (b) 585, (c), (d) 1020, (e), (f) 1508, and (g), (h) 1959. Symbols and color scheme for each data set are as documented in Table III. Dashed orange lines indicate  $z^+$  associated with the outer peak (i.e.,  $z_{OP}^+$ ).  $\Delta \overline{u^2}^+(z_{OP}^+)$  in (a), (c), (e), (g) corresponds to the attenuation in  $\overline{u^2}^+$  at  $z_{OP}^+$  as  $\Delta y^+$  increases from the well-resolved to worst-resolved scenario. White and green background in (b), (d), (f), and (h) indicate small-scale ( $\overline{u_L^2}^+$ ;  $\lambda_y^+ \leq 300$ ) and large-scale contributions ( $\overline{u_S^2}^+$ ;  $\lambda_y^+ > 300$ ), respectively.

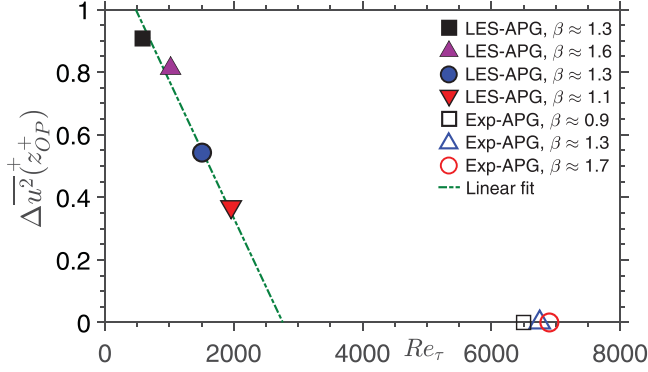


FIG. 9. Variation in attenuation of  $\overline{u^2}^+$  at  $z_{OP}^+$  [i.e.,  $\Delta \overline{u^2}^+(z_{OP}^+)$ ] with  $Re_\tau$ . Here  $\Delta \overline{u^2}^+(z_{OP}^+)$  is the difference between  $\overline{u^2}^+(z_{OP}^+)$  as  $\Delta y^+$  increases from the well-resolved to worst-resolved scenario (Tables II and III). Note that  $z_{OP}^+$  is assumed at  $0.3\delta_{90}^+$  for the Exp-APG data following Sanmiguel Vila *et al.* [30]. Dashed green line indicates linear fit based purely on the LES-APG data.

The  $Re_\tau$  trend in Fig. 9 can be explained based on the fact that the small-scale energy in the outer region reduces significantly as  $Re_\tau \gtrsim 6500$ . This is confirmed from the  $u$ -spectra contours associated with Exp-APG data sets in Figs. 10(d)–10(f), which indicate very low energy at small  $\lambda_x^+$  in the outer region. Consequently, increasing  $\Delta y^+$  only attenuates the small-scale energy in the inner region and negligibly influences the contours in the outer region. Apart from reaffirming the  $Re_\tau$  trend of the small-scale energy, the analysis presented in Figs. 8–10 also suggests negligible influence of spatial-resolution effects ( $l^+ \lesssim 60$ ) in the outer region of high  $Re_\tau$  APG TBLs ( $\gtrsim 3000$ ), at least for moderate  $\beta (\lesssim 2)$ . This is reassuring for past as well as future experimental studies investigating this parameter space, especially from the perspective of proposal and validation of new scaling arguments for the outer region. Present conclusion, however, adds additional challenges for correction schemes for APG TBLs (i.e., dependence on  $Re_\tau$ ,  $\beta$  and  $\bar{\beta}$ ), which in the case of ZPG TBLs have relied on the negligible small-scale energy variation with  $Re_\tau$  [37,43,45]. It is worth noting here that the present Exp-APG data set was acquired in a TBL with a well-controlled upstream history. Hence, it is possible that the negligible spatial-resolution effects noted here at  $Re_\tau \sim 7000$

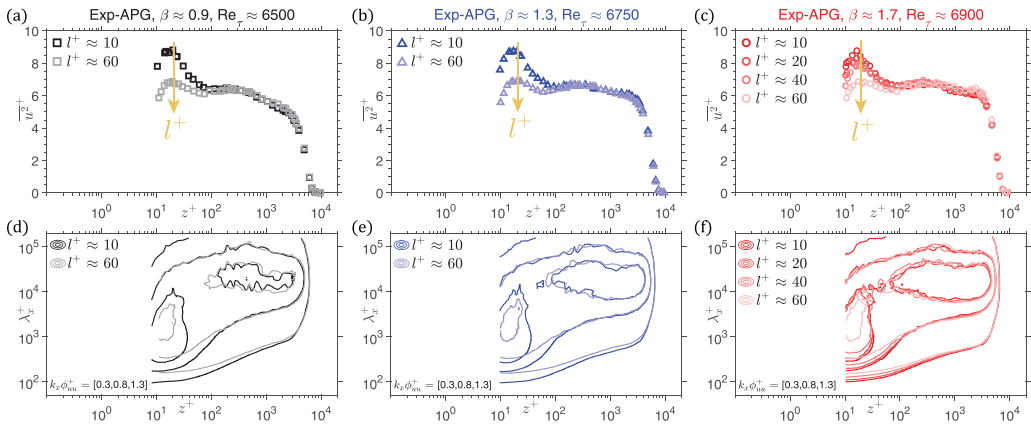


FIG. 10. (a)–(c) Streamwise turbulent-kinetic energy,  $\overline{u^2}^+$  and (d)–(f) constant-energy contours of premultiplied  $u$  spectra estimated for Exp-APG data sets with various spatial resolutions ( $l^+$ ) at  $\beta \approx$  (a), (d) 0.9, (b), (e) 1.3, and (c), (f) 1.7. Symbols and color scheme for each data set are as documented in Table II.

may be associated with the given upstream history. However, the  $Re_\tau$  trend demonstrated based on the LES-APG data set confirms that the spatial attenuation in the outer region does reduce with  $Re_\tau$ , and this is related to the reduction in small-scale energy with  $Re_\tau$ . Another aspect worth discussing here is the noticeable scatter in the  $\overline{u^2}^+$  profiles observed in Fig. 10(c) for Exp-APG data at  $\beta \approx 1.7$ . Based on close inspection of the repeated experiments at various  $l^+$ , we believe that this is owing to measurement uncertainty, which may decrease by increasing data-acquisition time, i.e.,  $TU_\infty/\delta_{99} > 20000$ . This, however, was not tested here due to the already very long acquisition time ( $T = 720$  s) used for each  $z^+$  location in Exp-APG, beyond which hotwire drift will likely be significant. This could be tested in future studies conducted at higher free-stream velocities.

## VI. CONCLUDING REMARKS

The present study investigates  $Re_\tau$  effects in the outer region of an APG TBL by analyzing data sets across a decade of  $Re_\tau$  ( $600 \lesssim Re_\tau \lesssim 7000$ ). The data are a combination of the well-resolved LES data set of Pozuelo *et al.* [8], corresponding to the low- $Re_\tau$  range, and new high- $Re_\tau$  experimental data from the Melbourne wind tunnel, both of which correspond to the moderate- $\beta$  range ( $\lesssim 2$ ). A unique aspect of the LES data set is the considerable  $Re_\tau$  range,  $1000 \lesssim Re_\tau \lesssim 2000$ , along which the APG TBL is allowed to develop at a nominally constant  $\beta \sim 1.4$ . This enables investigation of the  $Re_\tau$  effects with negligible influence of  $\beta$  and a very weak change in the upstream-history effects with  $x(\bar{\beta}(x))$ . In the case of the experimental data, on the other hand, the streamwise pressure gradient is set up based on the methodology of Clauser [4], wherein the APG TBL grows starting from a canonical TBL at  $Re_\tau \sim 4000$ , i.e., with no unique upstream-history effects. Analysis of these data is complemented using published data sets of ZPG TBLs, in the same  $Re_\tau$  range, to identify the unique trends associated with APG TBLs.

Scale-based decomposition of the streamwise normal stresses reveals that the viscous-scaled small-scale energy ( $\overline{u_S^2}^+$ ) in the outer region of an APG TBL decreases with  $Re_\tau$ , which is in contrast with quasi- $Re_\tau$  invariance depicted by these scales in ZPG TBLs. This conclusion provides a basis of support for the hypothesis of Tanarro *et al.* [28] that increasing Reynolds numbers lead to a decreasing influence of the APG effects. On the other hand, the large-scale energy ( $\overline{u_L^2}^+$ ) corresponding to attached eddies and superstructures is found to increase with  $Re_\tau$  across the entire TBL, for both the ZPG and APG case. The contrasting  $Re_\tau$  trends for  $\overline{u_S^2}^+$  and  $\overline{u_L^2}^+$ , in the case of APG TBLs, is deemed responsible for the indeterminate trend of  $\overline{u^2}^+$  profiles with  $Re_\tau$  [Fig. 5(b)]. To understand the origins of this phenomenon, the dominant term associated with production of turbulent kinetic energy,  $\overline{uw}^+(\partial U^+/\partial z^+)$ , is investigated across  $600 \lesssim Re_\tau \lesssim 2000$ . The analysis reveals that production of turbulence in the small scales decreases with  $Re_\tau$  in the outer region of an APG TBL, thereby explaining the decrease in  $\overline{u_S^2}^+$ . This decrease in small-scale production also (partly) explains the drop in the outer peak of the net production of turbulent kinetic energy, noted previously by Pozuelo *et al.* [8].

The  $Re_\tau$  effects on the small-scale energy are also confirmed by investigating the attenuation of  $\overline{u^2}^+$  by decreasing spanwise resolution (i.e., increasing  $\Delta y^+$  or  $l^+$ ), as a function of  $Re_\tau$ . The degree of attenuation of  $\overline{u^2}^+$  quantified at the outer peak location  $z_{OP}^+$ , albeit significant at low- $Re_\tau$  ( $\sim 1000$ ), was found to decrease with  $Re_\tau$  in a quasilinear manner. The trend suggested negligible energy attenuation in the outer region for  $Re_\tau \gtrsim 3000$ , which was tested by using hotwire data acquired for the nominally same spatial-resolution range. Experimental data at  $Re_\tau \gtrsim 6500$  confirmed negligible attenuation in  $\overline{u^2}^+$  in the outer region of a moderate APG TBL, reaffirming the  $Re_\tau$  effects on the small-scale energy concluded based on energy decomposition analysis. It would be interesting to assess whether a similar reduction in small-scale energy with  $Re_\tau$  is also noted for much higher  $\beta$  (where the flow characteristics are closer to a wall-confined wake [16,19,20]), and if these contributions become negligible at a much larger  $Re_\tau$  than present predictions. This study, hence,

informs future studies requiring high- $Re_\tau$  APG TBLs with negligible upstream-history effects. Potential projects include rigorously investigating changes in the log law (i.e.,  $\kappa$  and  $A$ , [7], which likely would require higher-fidelity  $U_\tau$  measurements) and testing scaling arguments for the outer peak [8,22,23] based on high- $Re_\tau$  data [ $\gtrsim O(10^4)$ ]. Present work confirms that high- $Re_\tau$  experiments in the outer region would have negligible errors due to spanwise spatial resolution (for moderate  $\beta \lesssim 2$  and modest  $l^+ \lesssim 60$ ), which is good news for these future experiments. The decrease in small-scale energy in the outer region with increasing  $Re_\tau$ , however, suggests that any new scaling arguments for APG TBLs should be rigorously tested across a broad range of  $Re_\tau$ .

#### ACKNOWLEDGMENTS

The authors are grateful to Dr. R. Pozuelo for sharing the LES data sets and acknowledge P. Manovski for helpful comments and suggestions on the manuscript. Financial support from the Australian Research Council is gratefully acknowledged. R.D. also acknowledges financial support by the University of Melbourne through the Melbourne Postdoctoral Fellowship. R.V. acknowledges the financial support from ERC Grant No. 2021-CoG-101043998, DEEPCONTROL. Views and opinions expressed are however those of the author(s) only and do not necessarily reflect those of the European Union or the European Research Council. Neither the European Union nor the granting authority can be held responsible for them.

The authors made the following contributions: R.D.: writing (original draft), conceptualization, supervision, methodology, validation, investigation, formal analysis; A.v.d.B.: writing (original draft), experiments, investigation, formal analysis, validation; R.V.: conceptualization, methodology, writing (review and editing), resources, investigation; L.L.: writing (review and editing), experimental setup; I.M.: supervision, conceptualization, writing (review and editing), funding acquisition.

The authors declare that they have no conflict of interest.

#### APPENDIX A: CONFIRMATION OF “CANONICAL” UPSTREAM CONDITION FOR EXP-APG

The high  $Re_\tau$  Exp-APG data set presented in this study is unique in the sense that the APG TBL develops from a well-established ZPG TBL at  $Re_\tau \sim 4000$ , as its initial condition (Sec. II). This is realized by controlling the outflow from the air bleeds for  $x < 9$  m of the test section, with outflow screens installed at the test-section outlet (nos. 1, 2, 3; Fig. 1). While the near-constant  $C_p$  distribution in Fig. 1(b) does indicate development of a canonical ZPG for  $x < 9$  m [1], here we reaffirm this claim by comparing streamwise velocity statistics measured at  $x \approx 8$  m for screen no. 3 configuration with those measured at matched conditions for screen no. 0 configuration [Fig. 11(a)]. Here the data for screen no. 0 configuration are from the published data set of Hutchins *et al.* [13], when there was no control on the air bleeds on the ceiling. The reasonable match of  $U^+$  and  $\overline{u'^2}^+$  profiles, obtained from the two different screen configurations, suggests that the TBL developing in the first  $\sim 9$  m (for screen no. 3 configuration) can be deemed as near canonical. This confirms that the APG TBL growing for  $x > 9$  m has a near-“canonical” upstream-history condition.

#### APPENDIX B: MEAN VELOCITY PROFILES FOR EXP-APG WITH VARYING SPATIAL RESOLUTIONS

It is already known [13] that the mean velocity profiles ( $U^+$ ) in a ZPG TBL are not influenced by changes in hotwire spatial resolution ( $l^+$ ) used for measurement. To confirm that the same is valid for APG TBL, Fig. 11(b) compares  $U^+$  profiles obtained at matched  $\beta$  and  $Re_\tau$  but for varying hotwire  $l^+$ . Indeed,  $U^+$  profiles collapse over one another, suggesting  $l^+ \lesssim 60$  doesn't influence the mean velocity profiles, at least in the moderate  $\beta (\lesssim 2)$  range considered.

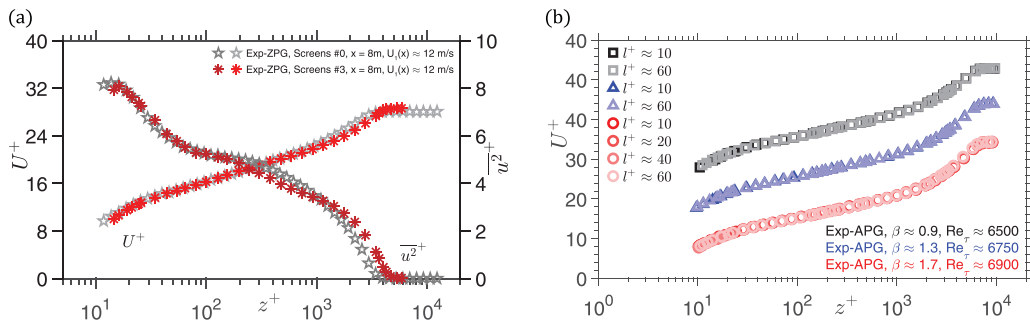


FIG. 11. (a)  $U^+$  and  $\overline{u^2}^+$  profiles measured in the Melbourne wind tunnel at matched  $x$  locations and free-stream velocity conditions for two different outflow screen configurations, Screen no. 0 and no. 3, as described in Sec. II. (b) Mean streamwise velocity profiles measured for high  $Re_\tau$  Exp-APG data sets with hotwires for various spatial resolutions ( $l^+$ ) at various  $\beta$ ,  $0.9 \lesssim \beta \lesssim 1.7$ . Symbols and color scheme for each data set are as documented in Table II. Data are separated by a shift in the  $U^+$  axis for clarity.

### APPENDIX C: ENERGY DECOMPOSITION INTO SMALL- AND LARGE-SCALE CONTRIBUTIONS

This Appendix reaffirms that the choice of  $\lambda_{y,c}^+ = 300$  is reasonable to decompose the streamwise normal stress ( $\overline{u^2}^+$ ) into small-scale ( $\overline{u_S^2}^+$ ;  $\lambda_y^+ \leq \lambda_{y,c}^+$ ) and large-scale contributions ( $\overline{u_L^2}^+$ ;  $\lambda_y^+ > \lambda_{y,c}^+$ ). To this end, Fig. 12 shows  $\overline{u^2}^+$  decomposed into  $\overline{u_L^2}^+$  and  $\overline{u_S^2}^+$  for the DNS data set of a turbulent channel flow [56]. Consistent with the previous knowledge on small-scale behavior [13],  $\overline{u_S^2}^+$  demonstrates convincing collapse across a decade of  $Re_\tau$ ,  $550 < Re_\tau < 5200$ , while  $\overline{u_L^2}^+$  increases with  $Re_\tau$ . Hence,  $\lambda_{y,c}^+ = 300$  seems a reasonable choice [57] to compare  $Re_\tau$  trends for  $\overline{u_S^2}^+$  and  $\overline{u_L^2}^+$  between ZPG and APG TBLs.

### APPENDIX D: INFLUENCE OF UPSTREAM-HISTORY EFFECTS ON SMALL-SCALE ENERGY

This Appendix is presented to reaffirm that the reduction in small-scale energy contributions to streamwise normal stress [Fig. 6(d)] and production of turbulent kinetic energy [Fig. 7(f)], discussed in Sec. IV, is not an artifact of upstream-history effects ( $\bar{\beta}$ ). To this end, Figs. 13(a) and 13(b) compare  $\overline{u_S^2}^+$  and  $-\overline{u_S w_S^+} \partial U^+ / \partial z^+$  estimated from the published LES data set of Bobke *et al.* [15] and Pozuelo *et al.* [8], at similar  $Re_\tau$  and  $\beta$  but different  $\bar{\beta}$ . It is evident from the comparison that both  $\overline{u_S^2}^+$  and  $-\overline{u_S w_S^+} \partial U^+ / \partial z^+$  increase in the outer region with increasing  $\bar{\beta}$ . This confirms the trend documented in Table I, based on our understanding of the literature [28]. Also, this trend

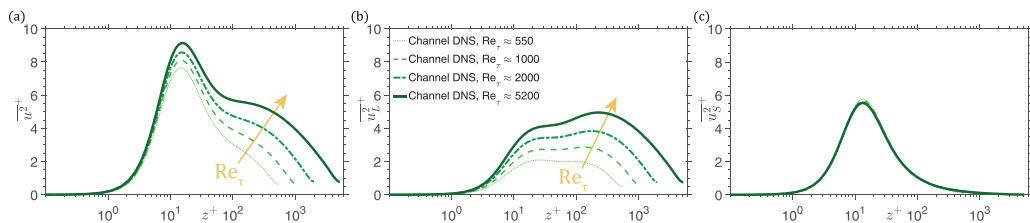


FIG. 12. (a)  $\overline{u^2}^+$  decomposed into (b) large-scale ( $\overline{u_L^2}^+$ ) and (c) small-scale contributions ( $\overline{u_S^2}^+$ ) for DNS data set of a turbulence channel flow [56] at various  $Re_\tau$ . Energy decomposition is based on using  $\lambda_{y,c}^+ = 300$ , the same as in Fig. 6.



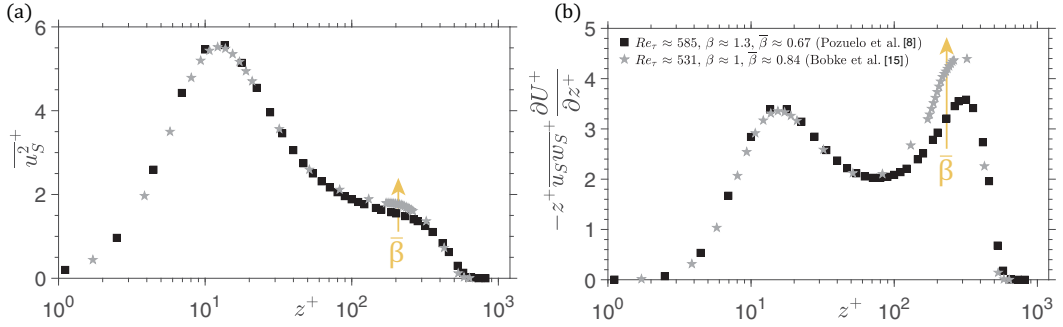


FIG. 13. Small-scale contribution to (a) streamwise normal stress ( $\overline{u_S^2}^+$ ) and (b) production of turbulent kinetic energy ( $-z^+ \overline{u_S w_S^+} \frac{\partial U^+}{\partial z^+}$ ) compared for LES data set of Bobke *et al.* [15] and Pozuelo *et al.* [8]. The comparison is made at similar  $Re_\tau$  and  $\beta$  but different  $\overline{\beta}$ , to understand the influence of upstream history. Spectral decomposition is based on  $\lambda_{y,c}^+ = 300$ . Estimates for the simulation data sets correspond to their original (i.e., well-resolved) grid resolution ( $\Delta y^+$ , Table III).

is opposite to what is noted on comparing various cases of LES-APG (Table III), suggesting that variation in upstream-history effects is weak. This confirms that the reduction in small-scale energy in the outer region of an APG TBL is purely a  $Re_\tau$  effect.

- 
- [1] F. H. Clauser, The turbulent boundary layer, *Adv. Appl. Mech.* **4**, 1 (1956).
  - [2] W. J. Devenport and K. T. Lowe, Equilibrium and non-equilibrium turbulent boundary layers, *Prog. Aerospace Sci.* **131**, 100807 (2022).
  - [3] R. Vinuesa, A. Bobke, R. Örlü, and P. Schlatter, On determining characteristic length scales in pressure-gradient turbulent boundary layers, *Phys. Fluids* **28**, 055101 (2016).
  - [4] F. H. Clauser, Turbulent boundary layers in adverse pressure gradients, *J. Aeronaut. Sci.* **21**, 91 (1954).
  - [5] D. Coles, The law of the wake in the turbulent boundary layer, *J. Fluid Mech.* **1**, 191 (1956).
  - [6] I. Marusic, J. P. Monty, M. Hultmark, and A. J. Smits, On the logarithmic region in wall turbulence, *J. Fluid Mech.* **716**, R3 (2013).
  - [7] T. Knopp, N. Reuther, M. Novara, D. Schanz, E. Schülein, A. Schröder, and C. Kähler, Experimental analysis of the log law at adverse pressure gradient, *J. Fluid Mech.* **918**, A17 (2021).
  - [8] R. Pozuelo, Q. Li, P. Schlatter, and R. Vinuesa, An adverse-pressure-gradient turbulent boundary layer with nearly constant  $\beta \simeq 1.4$  up to  $Re_\theta \simeq 8700$ , *J. Fluid Mech.* **939**, A34 (2022).
  - [9] P. E. Skaare and P.-Å. Krogstad, A turbulent equilibrium boundary layer near separation, *J. Fluid Mech.* **272**, 319 (1994).
  - [10] J. H. Lee, Large-scale motions in turbulent boundary layers subjected to adverse pressure gradients, *J. Fluid Mech.* **810**, 323 (2017).
  - [11] R. Vinuesa, P. S. Negi, M. Atzori, A. Hanifi, D. S. Henningson, and P. Schlatter, Turbulent boundary layers around wing sections up to  $Re_c = 1,000,000$ , *Int. J. Heat Fluid Flow* **72**, 86 (2018).
  - [12] M. Bross, T. Fuchs, and C. J. Kähler, Interaction of coherent flow structures in adverse pressure gradient turbulent boundary layers, *J. Fluid Mech.* **873**, 287 (2019).
  - [13] N. Hutchins, T. B. Nickels, I. Marusic, and M. S. Chong, Hot-wire spatial resolution issues in wall-bounded turbulence, *J. Fluid Mech.* **635**, 103 (2009).
  - [14] Z. Harun, J. P. Monty, R. Mathis, and I. Marusic, Pressure gradient effects on the large-scale structure of turbulent boundary layers, *J. Fluid Mech.* **715**, 477 (2013).

- [15] A. Bobke, R. Vinuesa, R. Örlü, and P. Schlatter, History effects and near equilibrium in adverse-pressure-gradient turbulent boundary layers, *J. Fluid Mech.* **820**, 667 (2017).
- [16] T. R. Gungor, Y. Maciel, and A. G. Gungor, Energy transfer mechanisms in adverse pressure gradient turbulent boundary layers: Production and inter-component redistribution, *J. Fluid Mech.* **948**, A5 (2022).
- [17] L. Castillo and W. K. George, Similarity analysis for turbulent boundary layer with pressure gradient: Outer flow, *AIAA J.* **39**, 41 (2001).
- [18] T. Knopp, N. Buchmann, D. Schanz, B. Eisfeld, C. Cierpka, R. Hain, A. Schröder, and C. J. Kähler, Investigation of scaling laws in a turbulent boundary layer flow with adverse pressure gradient using PIV, *J. Turbul.* **16**, 250 (2015).
- [19] V. Kitsios, C. Atkinson, J. A. Sillero, G. Borrell, A. Gungor, J. Jiménez, and J. Soria, Direct numerical simulation of a self-similar adverse pressure gradient turbulent boundary layer, *Int. J. Heat Fluid Flow* **61**, 129 (2016).
- [20] Y. Maciel, T. Wei, A. G. Gungor, and M. P. Simens, Outer scales and parameters of adverse-pressure-gradient turbulent boundary layers, *J. Fluid Mech.* **844**, 5 (2018).
- [21] T. Gibis, C. Wenzel, M. Kloker, and U. Rist, Self-similar compressible turbulent boundary layers with pressure gradients. Part 2. Self-similarity analysis of the outer layer, *J. Fluid Mech.* **880**, 284 (2019).
- [22] R. Pozuelo, Q. Li, P. Schlatter, and R. Vinuesa, Spectra of near-equilibrium adverse-pressure-gradient turbulent boundary layers, *Phys. Rev. Fluids* **8**, L022602 (2023).
- [23] T. Wei and T. Knopp, Outer scaling of the mean momentum equation for turbulent boundary layers under adverse pressure gradient, *J. Fluid Mech.* **958**, A9 (2023).
- [24] M. V. Zagarola and A. J. Smits, Mean-flow scaling of turbulent pipe flow, *J. Fluid Mech.* **373**, 33 (1998).
- [25] X. Chen and K. R. Sreenivasan, Reynolds number scaling of the peak turbulence intensity in wall flows, *J. Fluid Mech.* **908**, R3 (2021).
- [26] S. Romero, S. Zimmerman, J. Philip, C. White, and J. Klewicki, Properties of the inertial sublayer in adverse pressure-gradient turbulent boundary layers, *J. Fluid Mech.* **937**, A30 (2022).
- [27] J. P. Monty, Z. Harun, and I. Marusic, A parametric study of adverse pressure gradient turbulent boundary layers, *Int. J. Heat Fluid Flow* **32**, 575 (2011).
- [28] Á. Tanarro, R. Vinuesa, and P. Schlatter, Effect of adverse pressure gradients on turbulent wing boundary layers, *J. Fluid Mech.* **883**, A8 (2020).
- [29] C. Sanmiguel Vila, R. Örlü, R. Vinuesa, P. Schlatter, A. Ianiro, and S. Discetti, Adverse-pressure-gradient effects on turbulent boundary layers: Statistics and flow-field organization, *Flow, Turbul. Combust.* **99**, 589 (2017).
- [30] C. Sanmiguel Vila, R. Vinuesa, S. Discetti, A. Ianiro, P. Schlatter, and R. Örlü, Separating adverse-pressure-gradient and Reynolds-number effects in turbulent boundary layers, *Phys. Rev. Fluids* **5**, 064609 (2020).
- [31] R. Vinuesa, R. Örlü, C. Sanmiguel Vila, A. Ianiro, S. Discetti, and P. Schlatter, Revisiting history effects in adverse-pressure-gradient turbulent boundary layers, *Flow, Turbul. Combust.* **99**, 565 (2017).
- [32] C. Sanmiguel Vila, R. Vinuesa, S. Discetti, A. Ianiro, P. Schlatter, and R. Örlü, Experimental realisation of near-equilibrium adverse-pressure-gradient turbulent boundary layers, *Exp. Thermal Fluid Sci.* **112**, 109975 (2020).
- [33] A. Townsend, *The Structure of Turbulent Shear Flow*, 2nd ed. (Cambridge University Press, Cambridge, 1976).
- [34] A. Perry, I. Marusic, and M. Jones, On the streamwise evolution of turbulent boundary layers in arbitrary pressure gradients, *J. Fluid Mech.* **461**, 61 (2002).
- [35] A. Smits, B. McKeon, and I. Marusic, High-Reynolds number wall turbulence, *Annu. Rev. Fluid Mech.* **43**, 353 (2011).
- [36] I. Marušić and A. Perry, A wall-wake model for the turbulence structure of boundary layers. Part 2. Further experimental support, *J. Fluid Mech.* **298**, 389 (1995).
- [37] R. Deshpande, J. P. Monty, and I. Marusic, A scheme to correct the influence of calibration misalignment for cross-wire probes in turbulent shear flows, *Exp. Fluids* **61**, 85 (2020).

- [38] C. Cuvier, S. Srinath, M. Stanislas, J.-M. Foucaut, J.-P. Laval, C. Kähler, R. Hain, S. Scharnowski, A. Schröder, R. Geisler *et al.*, Extensive characterisation of a high Reynolds number decelerating boundary layer using advanced optical metrology, *J. Turbul.* **18**, 929 (2017).
- [39] C. D. Aubertine and J. K. Eaton, Turbulence development in a non-equilibrium turbulent boundary layer with mild adverse pressure gradient, *J. Fluid Mech.* **532**, 345 (1999).
- [40] R. J. Volino, Non-equilibrium development in turbulent boundary layers with changing pressure gradients, *J. Fluid Mech.* **897**, A2 (2020).
- [41] P. Ligrani and P. Bradshaw, Spatial resolution and measurement of turbulence in the viscous sublayer using subminiature hot-wire probes, *Exp. Fluids* **5**, 407 (1987).
- [42] P. Monkewitz, R. Duncan, and H. Nagib, Correcting hot-wire measurements of stream-wise turbulence intensity in boundary layers, *Phys. Fluids* **22**, 091701 (2010).
- [43] C. Chin, N. Hutchins, A. Ooi, and I. Marusic, Spatial resolution correction for hot-wire anemometry in wall turbulence, *Exp. Fluids* **50**, 1443 (2011).
- [44] A. Smits, J. Monty, M. Hultmark, S. C. C. Bailey, N. Hutchins, and I. Marusic, Spatial resolution correction for wall-bounded turbulence measurements, *J. Fluid Mech.* **676**, 41 (2011).
- [45] J. Lee, J. Monty, and N. Hutchins, Validating under-resolved turbulence intensities for PIV experiments in canonical wall-bounded turbulence, *Exp. Fluids* **57**, 1 (2016).
- [46] I. Marusic, K. Chauhan, V. Kulandaivelu, and N. Hutchins, Evolution of zero-pressure-gradient boundary layers from different tripping conditions, *J. Fluid Mech.* **783**, 379 (2015).
- [47] R. Vinuesa, P. H. Rozier, P. Schlatter, and H. M. Nagib, Experiments and computations of localized pressure gradients with different history effects, *AIAA J.* **52**, 368 (2014).
- [48] A. Drózdź, P. Niegodajew, M. Romańczyk, and W. Elsner, Effect of Reynolds number on turbulent boundary layer approaching separation, *Exp. Thermal Fluid Sci.* **125**, 110377 (2021).
- [49] A. E. Perry, *Hot-Wire Anemometry* (Oxford Science Publication, Oxford, 1982).
- [50] Y. Xia, W. A. Rowin, T. Jelly, I. Marusic, and N. Hutchins, Investigation of cold-wire spatial and temporal resolution issues in thermal turbulent boundary layers, *Int. J. Heat Fluid Flow* **94**, 108926 (2022).
- [51] K. Talluru, V. Kulandaivelu, N. Hutchins, and I. Marusic, A calibration technique to correct sensor drift issues in hot-wire anemometry, *Meas. Sci. Technol.* **25**, 105304 (2014).
- [52] G. Eitel-Amor, R. Örlü, and P. Schlatter, Simulation and validation of a spatially evolving turbulent boundary layer up to  $Re_\theta = 8300$ , *Int. J. Heat Fluid Flow* **47**, 57 (2014).
- [53] J. A. Sillero, J. Jiménez, and R. Moser, Two-point statistics for turbulent boundary layers and channels at Reynolds numbers up to  $\delta^+ \approx 2000$ , *Phys. Fluids* **26**, 105109 (2014).
- [54] T. Nickels, Inner scaling for wall-bounded flows subject to large pressure gradients, *J. Fluid Mech.* **521**, 217 (1999).
- [55] P.-Å. Krogstad and P. E. Skåre, Influence of a strong adverse pressure gradient on the turbulent structure in a boundary layer, *Phys. Fluids* **7**, 2014 (1995).
- [56] M. Lee and R. D. Moser, Direct numerical simulation of turbulent channel flow up to  $Re_\tau \approx 5200$ , *J. Fluid Mech.* **774**, 395 (2015).
- [57] M. Lee and R. D. Moser, Spectral analysis of the budget equation in turbulent channel flows at high Reynolds number, *J. Fluid Mech.* **860**, 886 (2019).
- [58] I. Marusic, R. Mathis, and N. Hutchins, High Reynolds number effects in wall turbulence, *Int. J. Heat Fluid Flow* **31**, 418 (2010).